# Properties of molecular clouds in MHD galaxy simulations

Rea Kontouli

Supervisor: Dr. Evangelia Ntormousi

Bachelor Thesis


Department of Physics

University of Crete

Greece

March 2022

# Abstract

In this work we investigate the possible effect of the magnetic field in star forming regions on galactic scales, using numerical simulations. We compare two identical models with only one difference, the one is magnetised and the other one is not. We find that there are differences in the gas distribution of the two galaxies that persist with time. The differences are more pronounced as time goes by. Also, the magnetised model forms slightly more dense gas and has a slightly higher star formation rate. In order to investigate this difference we turn to the molecular clouds and their properties. First, we identify the molecular clouds using three algorithms. We find out that the first two rely on resolution. Afterwards, we calculate the statistical properties of the clouds for both models looking for potential differences. We find that the properties are almost the same for the two models and consistent with observed molecular cloud scaling relations.

# Dedication

*To my mother, Eva, and Kostas who never stopped believing in me.*

# Acknowledgements

First and foremost, I would like to thank my supervisor Dr. Evangelia Ntormousi. This project would not have been possible without her support. Dr. Ntormousi has been not only an advisor but also a teacher and a mentor. She provided me with guidance in dark times of my undergraduate path. When I was coming across with obstacles in the academic or sentimental sector, she was always there for me. Furthermore, her insightful feedback pushed me to sharpen my thinking and brought my work to a higher level.

I would like to thank my mother for her financial and sentimental support throughout my studies. I would not be able to finish my studies without her support.

I would like to thank my friend and colleague Dimitris Kaltsas for not only for the productive collaboration throughout our studies, but also for the unlimited sentimental support that he provided. He was always there for me.

I would also like to acknowledge my committee members Professor Andreas Zezas and Dr. Carolina Casadio.

Last but not least, I would like to thank Dr. Kostas Kouroumpatzakis for his unlimited support and love. He helped me complete successfully my studies.

# Terminology

| | |
|---|---|
| SFR | Star Formation Rate |
| MHD | Magnetohydrodynamics |
| AMR | Adaptive Mesh Refinement |
| DICE | Disk Initial Conditions Environment |
| MCMC | Metropolis-Hasting Monte- Carlo Markov Chain |
| ISM | Interstellar Medium |
| GMCs | Giant molecular clouds |

Table 1: Acronyms

# Contents



[1]The contents of this chapter can be found in: Carroll, B. W.,& Ostlie, D. A. (2017). *An introduction to modern astrophysics*. Cambridge: Cambridge University Press.

# Chapter 1

# Introduction

## 1.1 The Interstellar medium components

### 1.1.1 Gas phases in the Interstellar Medium

The Interstellar medium (ISM) is the material that fills the space between stars in a galaxy. The ISM consists of gas, cosmic rays, magnetic fields and dust. In this work, we will be focusing on the gaseous component and the magnetic field, so we introduce their properties below.

We can identify four main phases of the interstellar gas, separated according to the temperature, density and ionization degree of the medium. These include (Kennicutt and Evans (2012)) the ionised medium with densities approximately less than $0.01cm^{-3}$ and temperatures higher than $10^5K$, the warm ionized medium (WIM) and the warm neutral medium with densities of range $0.1 - 1cm^{-3}$ and temperatures of several thousand Kelvins. The cold neutral medium (CNM) has densities higher than $10cm^{-3}$ and temperatures less than 100 K. The gas phases are summurised in the following table.

| **Gas phases** | | | | |
|---|---|---|---|---|
| | **Ionised Medium** | **Warm Ionised Medium (WIM)** | **Warm Neutral Medium** | **Cold Neutral Medium (CNM)** |
| **Density** | $< 0.01cm^{-3}$ | $0.1 - 1cm^{-3}$ | $0.1 - 1cm^{-3}$ | $> 10cm^{-3}$ |
| **Temperature** | $> 10^5K$ | $\sim 1000K$ | $\sim 1000K$ | $< 100K$ |

The cold neutral atomic phase of gaseous matter is traced by the hypefine transition line of hydrogen. The transition occurs at the wavelength of 21 cm.

The molecular gas is commonly traced by CO emission lines. Although the most abundant molecule in the interstellar medium is hydrogen, ($H_2$) it is not used as a tracer at low temperatures because it lacks a permanent dipole

moment, which means that dipole transitions between levels with different rotational and vibrational quantum numbers are forbidden.

Interstellar dust is also commonly used to trace the total gas column density, both in our Galaxy and in other galaxies (Kennicutt and Evans, 2012).Recently, a three-dimensional map of the local ISM was produced based on the reddening distribution along different lines of sight and stellar distances (Green et al., 2015). The amount of dust content of a galaxy is revealed via its interaction with photons emitted by the stars. Those photons are absorbed or scattered by the dust, creating the effect of interstellar extinction (Scicluna and Siebenmorgen, 2015).

The ISM contains objects characterized by Barnard (1908)[1] as "large areas of faint, diffused nebulous matter". Nowadays these structures are called *molecular clouds*. Their boundaries are defined by the detection of emission lines of CO or by the phenomenon of extinction of starlight due to the presence of dust.

## 1.2 Molecular clouds

Molecular clouds are an assemblage of dust and gas that can be found at the interstellar medium of galaxies. The conditions that govern these environments vary from cloud to cloud depending on many and diverse factors such as temperature, pressure, metal abundance, and magnetic fields.

With regard to morphology, the molecular clouds tend to be filamentary including smaller denser objects that are related to star formation (André et al. (2010),Men'shchikov et al. (2010),Williams et al. (2000)). Also, molecular clouds host supersonic motions (Zuckerman and Palmer (1974), Falgarone and Phillips (1990)), supersonic turbulence, that determines their substructure . Turbulence can affect the initial conditions of star formation procedure, when this process takes place creating smaller structures, called dense cores (Kritsuk et al., 2009).

*Diffuse molecular clouds* mainly contain hydrogen gas in atomic form. The molecular hydrogen can be found in regions of higher column density, where it may reach the value of $10^5 H_2$ molecules per cubic centimetre or more. In diffuse clouds, the temperature varies from 15 to 50 K, column density of hydrogen $n \sim 5 \times 10^8$ to $5 \times 10^9 m^{-3}$ and mass is $M \sim 3$ to $100 M_\odot$.

*Giant molecular clouds* (GMCs) are gigantic with sizes of the order of 50 pc across. The GMCs in our Galaxy are located in the spiral arms. Typical temperatures in their interiors are $T \sim 15K$, and number densities $n \sim 1 \times 10^8$ to $3 \times 10^9 m^{-3}$. and mass size typically about $M \sim 10^5$ to $10^6 M_\odot$.

GMCs display several substructures of locally greater density such as *dark cloud complexes, clumps, dense cores* and *hot cores.* The dark cloud complexes have sizes of order of 10 pc, masses of $10^4 M_\odot$, temperatures of $T \sim 10K$ and densities of $n \sim 5 \times 10^8 m^{-3}$. Smaller in scale are clumps with sizes in the order of a few parsecs, masses of $30 M_\odot$, temperatures of 10 K and densities of $n \sim 10^9 m^{-3}$. At even smaller scales are dense cores with sizes around 0.1 parsecs and masses of $10 M_\odot$. Their temperatures reach the value of 10 K

[1] Barnard *(1098), 177:231*

and their densities are $n \sim 10^10 m^{-3}$. According to Charnley (1995) hot cores are dense regions heated by young protostars. Typical sizes are 0.05 to 0.1 pc, masses $M \sim 10$ to $3000 M_\odot$, densities $n \sim 10^13$ to $3 \times 10^15 m^{-3}$ and temperatures $T \sim 100$ to 300 K.

Finally, *Bok globules* are dark and almost spherical clouds located outside of larger molecular complexes. Their sizes are less than 1 pc, they have masses of about $M \sim 1$ to $1000 M_\odot$, densities larger than $n \sim 10^{10} m^{-3}$ and low temperatures of 10 K.

### 1.2.1 Supernova feedback

Supernova feedback enriches the interstellar medium with hot gas (McKee and Ostriker, 1977). The supernova explosions provide the ISM with kinetic energy witch sometimes disembodies gas from clouds, and shock waves that disrupt the environment of clouds. The energy of the shocks can either compress the surrounding gas and lead to star formation or increase the kinetic energy of the molecules resulting of removing gas from the cloud.

## 1.3 The Schmidt-Kennicut law

One of the important questions related to the star formation process in the Universe is the rate at which galaxies form stars.

The Schmidt-Kennicutt law correlates the gas density with the star formation rate (SFR) of a galaxy. The relation was first examined by Maarten Schmidt (Schmidt, 1959). According to this relation, the SFR surface density should scale as some positive power of the local gas surface density, that is :

$$\Sigma_{SFR} \propto \Sigma_{gas}^{N} \tag{1.1}$$

Kennicutt (1998) used Ha, HI and CO emission lines distribution measurements of 61 spiral galaxies and far-infrared and CO observations of 36 of infrared-selected starburst galaxies. He found that the disk-averaged SFRs and gas densities for the combined sample are well represented by a Schmidt law with index $N = 1.4 \pm 0.15$ (Fig 1.1).

## 1.4 Larson relations

Larson (1981) derived empirical relations that relate the size, mass and velocity dispersion of Galactic molecular clouds. The first Larson's relation is illustrated in Figure 1.2 and defined by Eq.1.2.

$$\sigma(km \cdot s^{-1}) = 1.10 \cdot L(pc)^{0.38} \tag{1.2}$$

Moreover, Larson relates velocity dispersion with the mass of the cloud, as shown in Figure 1.3.

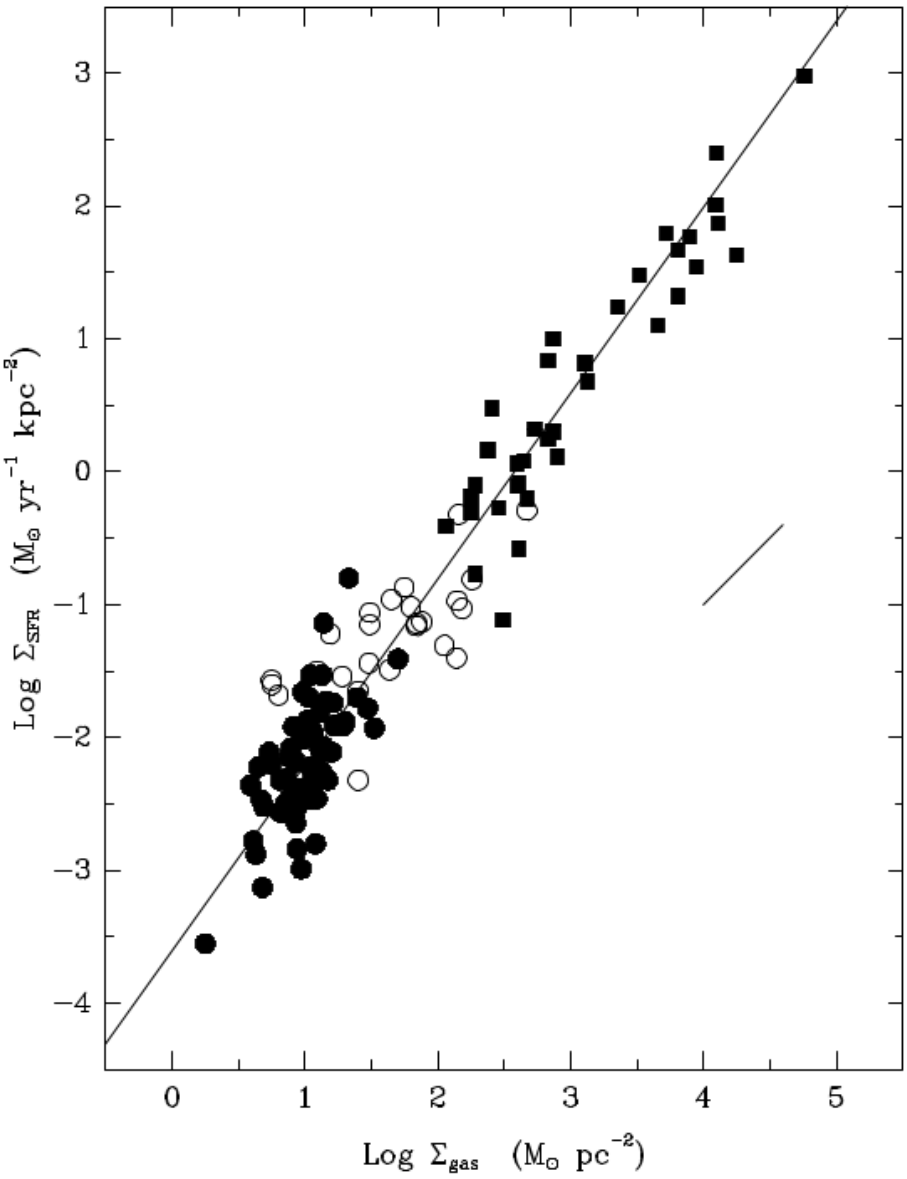


Figure 1.1: Data from Kennicutt (1998). Open circles show the SFRs and gas densities for the centers of the normal disk galaxies. The line is a least squares fit with index N = 1.40.

$$\sigma(km \cdot s^{-1}) = 0.42 \cdot M(M_\odot)^{0.20} \tag{1.3}$$

Finally, Larson

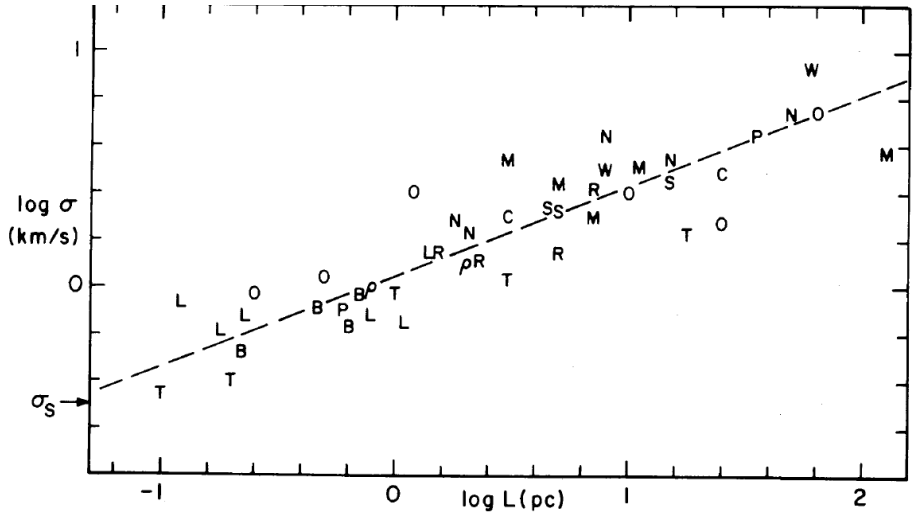


Figure 1.2: Relation between velocity dispersion and cloud size. Retrieved from Larson (1981).

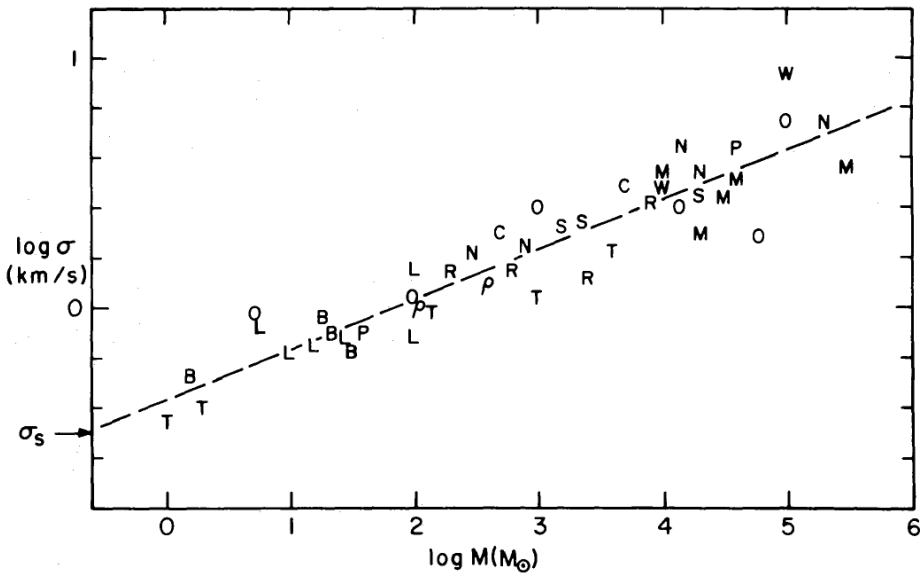


Figure 1.3: Relation between velocity dispersion and cloud mass. Retrieved from Larson (1981).

found that cloud size is inversely proportional to density (Fig.1.4).

$$\langle n_{H_2} \rangle (cm^{-3}) = 3400 \cdot L(pc)^{-1.10} \tag{1.4}$$

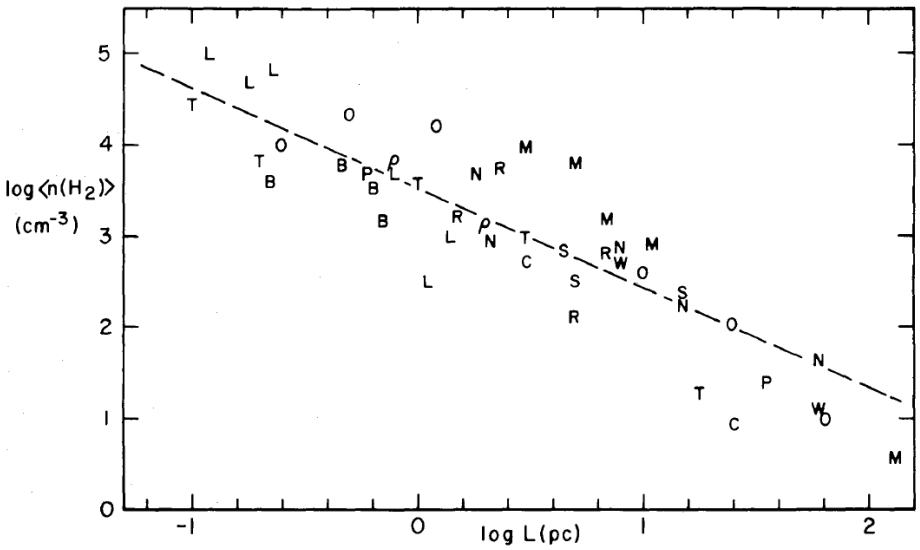


Figure 1.4: Relation between column density and cloud size. Retrieved from Larson (1981).

## 1.5 Gravitational Collapse[2]

Star formation happens in dense cores and globules in molecular clouds (Massi et al., 2019). Conditions that trigger gravitational collapse are still under study. The first who examined this problem was Sir James Jeans in 1902 (Jeans, 1902). He neglected effects due to rotation, turbulence and galactic magnetic fields and considered the collapse as a deviation from hydrostatic equilibrium. Here, we can approximate Jeans's result by starting from the virial equilibrium of a gravitationally bound system. The equilibrium condition is then described by the expression:

$$2K + U = 0 \tag{1.5}$$

where $K$ is the total internal kinetic energy of a molecular cloud, that is the kinetic energy of the motion of gas molecules and $U$ is the gravitational potential energy. The condition for collapse is the force due to gravitational pressure to exceed the force due to gas pressure. By importing the appropriate expression for the gravitational and kinetic energy of a spherical cloud of constant density into eq.1.5 and solve for the mass then this mass is the minimum mass necessary for the cloud to collapse (now commonly referred to as the *Jeans Mass* (1.6)).

$$M_J \simeq \left(\frac{5kT}{G\mu m_H}\right)^{3/2} \cdot \left(\frac{3}{4\pi\rho_o}\right)^{1/2} \tag{1.6}$$

[2]The contents of this chapter can be found in: Carroll, B. W.,& Ostlie, D. A. (2017). *An introduction to modern astrophysics*. Cambridge: Cambridge University Press.

where $k$ is Boltzman's constant, $T$ is the temperature, G the gravitational constant, $\mu$ the molecular weight, $m_H$ the hydrogen mass and $\rho_o$ is the cloud's initial density.

Assuming that any external pressure is negligible, the cloud performs free-fall. Throughout this phase the temperature of the gas remains constant, so the collapse is *isothermal*.

Considering a spherical cloud with constant density, the collapse can be described by the equation of hydrodynamic equilibrium.

$$\frac{d^2r}{dt^2} = -G\frac{M_r}{r^2} \tag{1.7}$$

where $r$ is the distance from the center, $G$ the gravitational constant and $M_r$ the mass enclosed by the sphere of radius $r$.

Equation 1.7 can be solved for a collapsing cloud with the Jeans Mass and calculate the free-fall timescale. The result is independent of the initial radius of the sphere and so the collapse is called *homologous*, that is for an originally uniform density, all parts of the cloud will take the same amount of time to collapse and the density will increase at the same rate everywhere.

However, if the central region of the cloud is more condensed when the collapse begins, the free- fall time will be shorter in this region. Moreover, the density in the very same region will increase more rapidly. In this case the collapse is called *inside-out collapse*.

### 1.5.1 Virial parameter

An important criterion for gravitational collapse to occur, is if the cloud, or the clump, core and globule is in such condition that gravity is able to dominate. In other words if the cloud exeeds the virial equilibrium. This means that the gravitationally bound state ceases and gravity prevails. The level of boundness of the cloud according to Bertoldi and McKee (1992) is expressed by the *virial parameter*.

The virial parameter is the ratio of the cloud's kinetic energy to its gravitational energy.

$$a_{virial} = \frac{5\sigma^2 R}{GM} \tag{1.8}$$

where $\sigma$ is the velocity dispersion, $R$ the radius of the cloud, $G$ the gravitational constant and $M$ the mass of the cloud.

## 1.6 Fragmentation

When an ISM structure satisfies the Jeans Criterion, then the collapse process begins. However, as we have mentioned above, GMCs are not uniform structures: they have hierarchically organized density distributions, with dense

filaments and cores within the more diffuse, extended cloud. They are also turbulent and magnetized, which means that the virial parameter is not uniform within a GMC, either. Therefore, different regions of the cloud will become gravitationally unstable independently, and a GMC will form multiple stars instead of collapsing monolithically.

In reality, collapsing clouds undergo *fragmentation*. During the free-fall phase of the collapse, the cloud's density increases by many orders of magnitude. In case the collapse is isothermal, the Jeans Mass has to decrease, according to eq.1.6. Consequently, if a region in the cloud locally satisfies the Jeans Criterion, depending on the local density, it will collapse forming smaller dense objects.

However, obeservations show that stars in galaxies have masses approximately smaller than a solar mass. This means that fragmentation has a limit.

Actually, the collapse does not always remain isothermal during the process because the energy that is released cannot always be radiated away efficiently. In this case, the temperature must rise and the collapse is called *adiabatic*. But if the temperature changes from eq.1.6, it can be assumed that the Jeans Mass will be affected.

The adiabatic law correlates gas pressure with the volume:

$$P \cdot V^{\gamma} = constant \tag{1.9}$$

where $P$ is the pressure, $V$ is the volume and $\gamma$ is the ratio of specific heats. Using the adiabatic law and the ideal gas law 1.10,it is obtained a relation between temperature and density 1.11.

$$P = \frac{nRT}{V} \tag{1.10}$$

where $P$ is the pressure, $V$ the volume, $n$ is the number of particles per volume and $T$ is the temperature.

$$T = C\rho^{\gamma-1} \tag{1.11}$$

where $C$ is a constant.

Substituting equation1.11 into eq.1.6, arises an adiabatic relation between Jeans Mass and density (eq.1.12).

$$M_J \propto \rho^{\frac{3\gamma-4}{2}} \tag{1.12}$$

Molecular clouds are abundant in atomic hydrogen. For atomic hydrogen $\gamma$ equals to 5/3, so from eq.1.12 Jeans Mass becomes:

$$M_J \propto \rho^{\frac{1}{2}} \tag{1.13}$$

From Eq.1.13 is assumed that there is a minimum mass for the fragments that will be produced during the adiabatic collapse. This mass is given by the relation :

$$M_{Jmin} = 0.03 \left( \frac{T^{1/4}}{e^{1/2}\mu^{9/4}} \right) M_{\odot} \tag{1.14}$$

where $M_{Jmin}$ is the minimum obtainable Jeans Mass, $T$ is the temperature, $e$ is an efficiency factor that declares the deviation from thermodynamic equilibrium, $\mu$ is the molecular weight and $M_{\odot}$ is the mass of the sun. Considered the moment that adiabatic collapse has begun, and suppose the values of $e \sim 0.1$, $\mu \sim 1$ and $T \sim 1000K$ then $M_J \sim 0.5M_{\odot}$. This means that fragmentation stops when the fragments reach approximately the mass of order of solar mass and gravitational collapse begins.

## 1.7 The Interstellar magnetic field

There are many processes, except from gravity, that play a role in the star formation circle. One of them is the magnetic field. Observationally, it is a challenge to measure the interstellar magnetic field because because its interaction with the radiation is weak. However, by simulating the magnetized ISM it is possible to control all the parameters than cannot be operated in observations.

The ISM can be described by the equations of magnetohydrodynamics (MHD) which are presented below.

$$\frac{\partial \rho}{\partial t} + \nabla \cdot (\rho u) = 0 \tag{1.15}$$

$$\rho \left( \frac{\partial \rho}{\partial t} + (u \cdot \nabla) u \right) = -\nabla P + \frac{(\nabla \times B) \times B}{4\pi} \tag{1.16}$$

$$\rho \left( \frac{\partial e}{\partial t} + (u \cdot \nabla) e \right) = -P(\nabla \cdot u) - \rho \mathcal{L} \tag{1.17}$$

$$\frac{\partial B}{\partial t} = \nabla \times (u \times B) \tag{1.18}$$

where $\rho$ is the mass density, $u$ is the velocity field, $P$ is the pressure, $B$ is the magnetic field, $e$ is the charge of the fluid and $\mathcal{L}$ is the net loss function and describes the radiative heating and cooling of the gas. But for the sake of completeness, the gas must be described by an equation of state. ISM can be considered as a perfect gas and described by an adiabatic equation of state:

$$P = (\gamma - 1)\rho e \tag{1.19}$$

where $\gamma$ is the adiabatic index of the gas. For monoatomic gas $\gamma = 5/3$.

## 1.8 Alfvén velocity

Even though molecular clouds are neutral overall, a small degree of ionization couples the magnetic field to the gas. This means that MHD is the correct framework for the description of these structures. The characteristic speed at which an MHD wave propagates in the plasma is the Alfvén speed:

$$u_A = \frac{B}{\sqrt{4\pi n_i m_i}} \tag{1.20}$$

where $B$ is the magnetic field, $n_i$ the ion number density and $m_i$ the ion mass.

## 1.9 Mass-to-flux ratio

Crutcher (1999) conducted measurements of the Zeeman effect in molecular clouds in order to measure the magnetic intensity. He found that the magnetic and kinetic energy in clouds are in the same order of magnitude. So, there is a critical mass for which the two energies equate. According to Mouschovias and Spitzer (1976) a clump resists gravitational collapse as long as its mass is less than a critical value $M_{critical}$ which is defined as follows:

$$M_{critical} = c_J M_J \left(1 - \left(\frac{M_\Phi}{M_{critical}}\right)^2\right)^{-3/2} \tag{1.21}$$

where $c_J$ is a numerical constant, $M_J$ is the Jean's Mass and $M_\Phi$ is the maximum mass a magnetised cloud can have while avoiding collapse.

$$M_\Phi = 0.12\Phi/G^{1/2} \tag{1.22}$$

where $\Phi$ is the magnetic flux $\Phi = \pi R^2 \overline{\mathrm{B}}$. The magnetic critical mass $M_\Phi$ can be used to define the mass-to-flux ration $\mu$. which is defined as the ratio between the magnetic critical mass and the magnetic flux, that is $\mu = M/\Phi$. When $\mu$ is greater than unity, $\mu > 1$, then the cloud is called magnetically *supercritical* and can resist collapse. On the contrary, when $\mu$ is lower than unity, $\mu < 1$ then the cloud is *subcritical* and cannot collapse. According to Hennebelle and Inutsuka (2019),

the gas in dense regions is magnetically supercritical.

## 1.10 Magnetic fields in spiral galaxies

### 1.10.1 Morphology of Milky-Way-like galaxies

The Milky Way is a spiral galaxy. Its components are the same in all spirals with some differences in structural characteristics. Milky-Way like galaxies[3] consist

[3]The information concerning the structure of spirals are derived from the book: *Extra-galactic Astronomy and Cosmology. An Introduction.* Peter Schneider, *Springer.*

of a *thin disk* of stars and gas with scale height of a few parcecs and scale length of a few kiloparsecs, a *thick disk* with a different stellar population than that of the thin disk, and a *bulge* which is located at the center. Finally, an almost spherical halo which consists of globular clusters and old stars surrounds the galaxy.

The spiral density waves of late-type galaxies like our own are characterised by high gas and dust densities, and contain young O and B stars. This observation indicates that they are sites of on-going star formation.

Galaxy evolution is strongly tied to to star formation. Among other processes, the magnetic field evolution plays an important role to the evolution of galaxies (Ntormousi (2018), Kudoh and Basu (2008), Beck et al. (1996). Observationally, the magnetic field intensity can be measured along the line of sight by Zeeman effect (Kazes et al., 1988) at subgalactic scales. At galactic scales, magnetic field can be measured using the effect of Faraday rotation from linearly polarized radio sources (Simard-Normandin and Kronberg (1980), Han and Zhang (2007)), and sychnotron emission (Beuermann et al. (1985), Miville-Deschênes et al. (2008)). On the other hand, polarized radiation is useful for studying the morphology of the magnetic field projected on the plane of the sky (Soler et al., 2013).

### 1.10.2 Magnetic field evolution

At the early Universe, the magnitude of magnetic fields did not exceed the value of $10^{-9} Gauss$ (Rees, 1987). On the other hand, local obeservations reveal that the magnetic field intensity of spiral galaxies is of the order of a few $\mu$G (Niklas (1995)), reaching tens of $\mu$G in and around spiral arms (Beck, 1991; Fletcher et al., 2011)

The difference between the primordial and present magnetic fields implies that the magnetic intensity underwent an amplification process. Amplifying the magnetic field intensity possibly affects the morphology and evolution of spiral galaxies.

Such an amplification can be sustained over time through a dynamo mechanism Rees (1987). Spiral galaxies rotate deferentially. This movement is able to create turbulence in the galactic plane that is capable to amplify magnetic lines in the galactic halo. Avoiding the challenges of observational measurements of magnetic field, simulations provide a more controllable environment. The work of Ntormousi et al. (2020) describes very well the mean field dynamo theory applied in a spiral galaxy. A poloidal component of magnetic field is created by a toroidal one and vice versa. As a result the magnetic intensity grows as the galaxy evolves in time. The growth of magnetic intensity found Ntormousi (2018) who simulated two models of a Milky Way like galaxy the one with poloidal and the other with toroidal magnetic field and studied the evolution of the magnetic field. The result was that regardless the initial morphology, a random magnetic field component is developed.

# Purpose

The purpose of this study is to investigate the effect of the magnetic field on the dense gas distribution and properties.

# Chapter 2

# Methods

## 2.1 Simulations

In this study we investigate the way the magnetic field affects the cloud properties and the star formation rate of an evolving galaxy through time. In order to do so, we use numerical simulations of Milky-Way-like galaxies that include a wide range of physical processes, described in Ntormousi et al. (2020). These simulations include dark matter and stars as collissionless components, as well as the multi-phase gaseous ISM, described in the Introduction. In this study, we compare two models of the simulated galaxy: Model M from Ntormousi et al. (2020), hereafter called *model MHD*, and an identical model without a magnetic field, hereafter *model HYDRO*.

The simulations were performed with RAMSES, , a non-commercial free fluid dynamics code (Teyssier (2002) ). RAMSES is a Cartesian grid code based on the Adaptive Mesh Refinement (AMR) technique, with a tree-based data structure. The base of the tree structure is called the coarse grid. The coarse grid represents the whole computational domain which acts like a unit cube. The refinement process starts from the coarse grid and continues to a maximum level of refinement, $l_{max}$, according to some user-defined refinement criterion. The user can determine the resolution by setting the size of the coarse grid and $l_{max}$. For a cubic grid at the maximum resolution, the computational volume is resolved by $2^{l_{max}}$ cells in each direction.

After the refinement of a cell, a new oct is created and the volume-averaged variables, such as the density and the velocity, are calculated at its center. While the density and velocity are defined at the center of the cell, the magnetic field is defined at the faces of the cells. So, the magnetic field has to be expressed as a volume-averaged component (Fromang et al., 2006). The MHD solver is based on the Constrained Transport scheme, which ensures a vanishing magnetic field divergence.

The equations that are solved by the code for both sets of simulations, are presented below:

$$\frac{\partial \rho}{\partial t} + \nabla \rho \cdot \mathbf{v} = \mathbf{0} \tag{2.1}$$

$$\frac{\partial \mathbf{v}}{\partial t} + (\mathbf{v} \cdot \nabla) \cdot \nabla + \frac{1}{\rho} \cdot \nabla \mathbf{P} = -\nabla \phi \tag{2.2}$$

$$\frac{\partial E_{tot}}{\partial t} + \nabla (E_{tot} + P)\mathbf{v} - (\mathbf{v} \cdot \mathbf{B}) \cdot \mathbf{B} = -\mathbf{v} \cdot \nabla \phi \tag{2.3}$$

$$\frac{\partial \mathbf{B}}{\partial t} - \nabla \times (\mathbf{v} \times \mathbf{B}) = \mathbf{0} \tag{2.4}$$

$$\nabla \cdot \mathbf{B} = \mathbf{0} \tag{2.5}$$

where $\rho$ is the density of the fluid,, $\mathbf{B}$ the magnetic field, $\mathbf{v}$ the velocity field and $\phi$ the gravitational potential. $\mathbf{P}$ is the pressure and is the sum of thermal and magnetic pressure.

$$P_{tot} = P + \frac{\mathbf{B} \cdot \mathbf{B}}{2} \tag{2.6}$$

We consider an ideal gas so the equation of state that closes the system is:

$$P = (\gamma - 1)\epsilon \tag{2.7}$$

where $\epsilon$ is the internal energy.
$E_{tot}$ is the total energy:

$$E_{tot} = \epsilon + \rho \frac{\mathbf{v} \cdot \mathbf{v}}{2} + \frac{\mathbf{B} \cdot \mathbf{B}}{2} \tag{2.8}$$

The gravitational potential stands for the stars and dark matter which are included in the simulations and are coupled with the gas as Eq.2.2 and 2.3 denote.

In order to simulate star formation, we use the native RAMSES star particle creation algorithm. Whenever certain user-defined criteria, such as a density threshold, are met, the algorithm turns gas that is gravitationally unstable into a collisionless particle. In the models we study here, the density threshold to form a star particle was set to $\rho_{thresh} = 1 cm^{-3}$. The conversion from gas to stellar mass is done with a user-set efficiency. Due to the limited resolution, in galaxy-scale simulations that particle is usually as massive as an entire stellar population. Stellar particles formed after the beginning of the simulation are assigned a positive age, while stellar particles used in the initial conditions have a negative age.

### 2.1.1 Numerical setup

The initial conditions for both simulations were created by DICE (Disk Initial Conditions Environment), an open-source, Monte-Carlo Markov Chain (MCMC) code (Perret et al., 2014; Perret, 2016). DICE uses Lagrangian particles to build the distributions of the different galaxy components and checks for hydrostatic equilibrium.

The simulated galaxies are Milky-Way analogues at $z = 0$: they both have a total mass of $M_{tot} = 2 \cdot 10^{12} M_{\odot}$ and a virial velocity 200 $km/sec$. The two models are simulated by an ideal hydrodynamical fluid described by the MHD equations, a dark matter component, and a stellar component, described as Lagrangian collisionless particles The mass fractions of dark, stellar and gaseous matter have the following values : 98.5%, represented by 2 million particles, 1.425%, represented by 1 million particles and 0.075% , respectively.

The density profile of the dark matter halo follows Navarro, Frenk & White (NFW) (Eq.2.9) (Navarro et al. (1996)).

$$\rho(r) \propto \frac{1}{r(1 + r/r_s)^2} \tag{2.9}$$

where $r_s$ is the scale radius. Here, the scale length is set to 3 kpc. Another quantity related to the NFW profile, is the half-mass radius. Because the NFW mass diverges, the half-mass radius is defined within a cut-off radius (Lokas and Mamon (2001)). Here the cut-off radius is 100 kpc. The stars and gas follow an exponential disk profile: the stellar disk has a scale length of 3 kpc and a cutoff of 12 kpc, while the gas has a scale length of 4kpc with a cutoff of 15 kpc. The gas temperature is set to 10,000 K, with no initial turbulent field.

Model MHD has an initial magnetic field with central strength of $0.1 \mu G$. Also, it is toroidal with a scale height and scale length of 1 kpc.

A crucial factor in star formation is the cooling and heating processes of the interstellar medium (see Introduction). We used the heating and cooling rates from Sutherland and Dopita (1993).

The AMR is used to study the evolution of the galaxy for both simulations. Starting with a coarse grid of $128^3$ and activating three nested levels of refinement at the location of the galaxy, the simulations reach a resolution of 1024 cells in each direction. By further activating two additional levels of refinement whenever a cell exceeds $100 particles cm^3$, the models reach a maximum effective resolution of $4096^3$ cells.

### 2.1.2 PyMSES

The post-processing of the simulations was largely performed using PyMSES [1]. PyMSES is a set of Python modules written for RAMSES.

[1] irfu.cea.fr/Projets/PYMSES

### 2.1.3 PyMSES visualisation tools

The first step of the data processing was to visualise the column density structure of the two models, which is expressed in units of atomic hydrogen.

The visualisation set up for the computed density structure, was operated by the PyMSES visualisation tool called *Camera*, which allows the creation of ray-traced maps.

The *Camera* tool accepts several parameters for the map creation. The *center* parameter determines the position from which the ray-tracing starts, here chosen to be a plane outside the galaxy, right above the galactic center. The *line of sight axis* parameter marks the axis of integration, chosen here to be the z-axis. Finally, *region size* determines the magnification of the map. Figure 2.1 describes the Camera features.

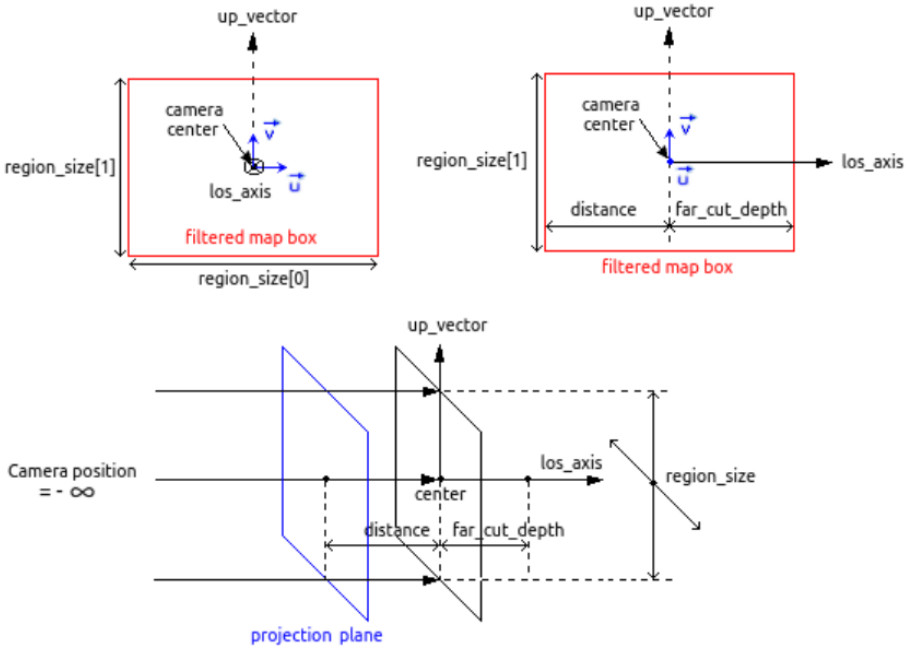


Figure 2.1: Camera visualisation tool. Credits to: http://irfu.cea.fr/Projets/PYMSES/ug_visu_camera.html

The Camera tool described above is combined with a a physical operator, which could be scalar or vector, to produce the ray-traced map of the desired quantity. Here, we use the density operator for column density maps, as well as velocity and magnetic field operators to visualise the corresponding projected vector fields.

In RAMSES, the magnetic fields are defined on cell edges, so that the output includes a left ($B_l$) and a right ($B_r$) component. Therefore, in order to compute

the magnetic field $B$ in the center of the cubic element, we calculate the mean magnetic field that is,

$$B_{tot} = \frac{B_r + B_l}{2} \tag{2.10}$$

As it was mentioned above, we simulate an interstellar medium as a magnetised fluid that is described by MHD equations. The medium complies with the continuity equation Eq.(2.1) therefore the ions oscillate with phase velocity, the $Alfvén$ velocity.

### 2.1.4 Identifying molecular clouds and properties

After visualising the density structure of the galaxy, the next step was to identify the molecular clouds and calculate their statistical properties. For this reason, we run three different algorithms which are described in the next subsections.

### 2.1.5 PyCupid

We used the Clumpfind algorithm as implemented in the Pycupid package. PyCupid [2] is a Python Wrapper functions for Starlink's CUPID[3] package, a software that provides a set of commands that identify and analyse clumps within two- and three- dimensional data arrays.

ClumpFind takes as input a two- or three-dimensional data array and contours it at many different levels starting from a value close to the peak array value and lowers it till a specified minimum contour level. At each contour level, all adjacent areas of pixels above the contour level, are found and identified as clumps. If that set already contains clumps, then the whole set is considered as a new clump.

ClumpFind contains some configuration parameters that control the clump selection process:

*DELTAT* represents the gap between the contour levels and expressed in terms of root mean square (RMS) noise.

*FWHMBEAM* is the full width at half maximum of the instrument beam, in pixels.

*MINPIX* is the lowest number of pixels a clump can contain. If a candidate clump has fewer than this number of pixels, it will be ignored. This prevents noise spikes from being interpreted as real clumps.

The values we used in our analysis for ClumpFind are : DELTAT = 1.0 * RMS, FWHMBEAM = 1, MINPIX = 8.

As an example, Figure 2.2 shows the clumps identified by Clumpfind in one of the simulated galaxies. The black contours correspond to Clumpfind. The red contours correspond to Fellwalker, another Pycupid's algorithm that is not used in the cloud identification and was used only provisionally for this plot.

[2] https://pycupid.readthedocs.io/en/latest/index.html
[3] http://starlink.eao.hawaii.edu/starlink/CUPID

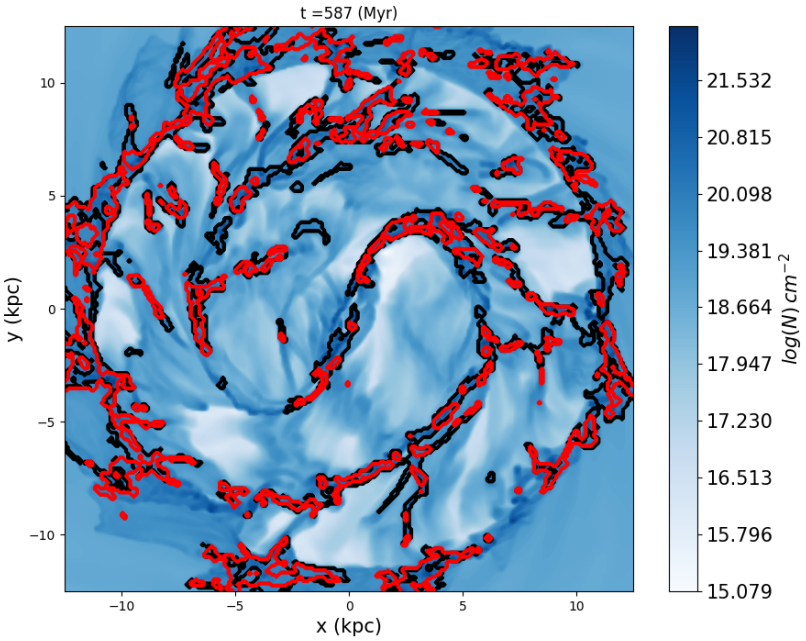


Figure 2.2: Density contour plot of the galaxy at evolution time of 587 Myrs, applying Pycupid. Clumpfind is represented by black contours.

### 2.1.6 Astrodendro

Astrodendro [4] is a python package that generates dendrograms for astronomical data.

A *dendrogram* uses a tree analogy to represent structures in data. Just like a tree, it is constructed by leaves, branches and trunks. As Figure 2.3 shows, branches split into leaves. The way the algorithm works is to construct the tree starting from the brightest pixels in the dataset. Then the algorithm continues to the next pixel with the largest value. If it is local maximum, a new structure is created. If not, then it is added to the previous structure. When the process is completed the structures merge into a tree. In this project, we apply this algorithm in the gas density of AMR data, so the brightest pixels correspond to those with the highest density.

There are several parameters that can control and set limits to the dendrogram computation. Below we describe those that were used in the analysis.

In order to avoid interpreting noise as structures, a minimum value (here equal to 0.01) is defined below which the tree structure cannot expand.

[4] https://dendrograms.readthedocs.io/en/stable/index.html

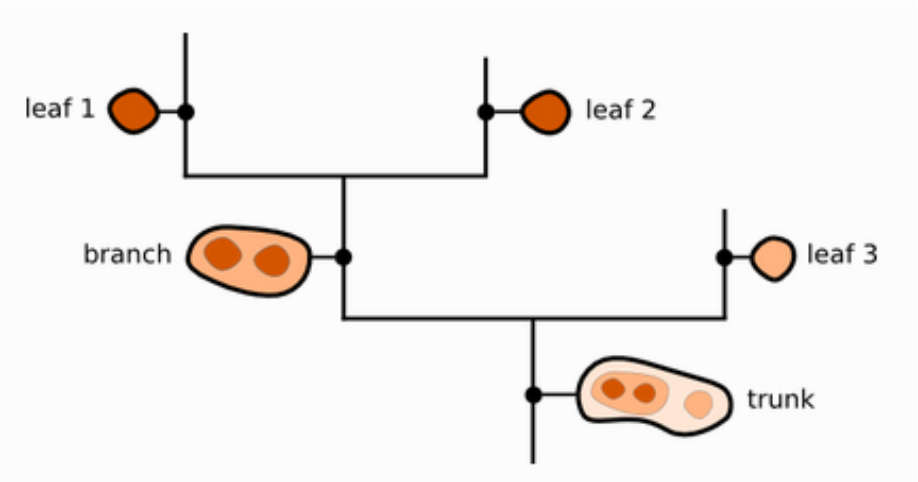


Figure 2.3: Dendrogram structure. Credits to: https://dendrograms.readthedocs.io/en/stable/index.html

Also, there is an option which determines the minimum value for a peak to be identified as structure. This is controlled by *min delta* option and with given value 1 in our analysis.

Finally, we set a minimum number of pixel that a structure should contain in order to remain independent. A leaf corresponds to the brightest pixel so in our case to the local densest region therefore, a cloud. This value is set to 16.

Figure2.4 shows the clouds that are found by dendrogram in the M model galaxy.

One weakness of the Astrodendro and Clumpfind implementations used here is that they need to be applied to uniformly spaced 3D data. Since RAMSES provides data on an irregularly spaced mesh (due to the usage of AMR), the simulation outputs had to be interpolated onto a regular grid before applying the clump-finding algorithms. As we will show in Chapter 3, this step introduces a dependency on the chosen resolution of the uniform grid. For this reason, we used an other algorithm, called HOP, which works directly on the AMR data, and is described in the following section.

### 2.1.7 HOP

Ultimately, we used HOP algorithm to identify molecular clouds. The HOP algorithm (Eisenstein and Hut, 1998) identifies groups of cells that belong to the three-dimensional grid in N-body simulations. The first step is to give each cell an estimation about the local density and then the algorithm links each cell to it's densest neighbor. The cells that reach the same maximum density value belong to the same group. This process is repeated till the cell with the greatest density reaches itself. For this reason it is a converging method. If a

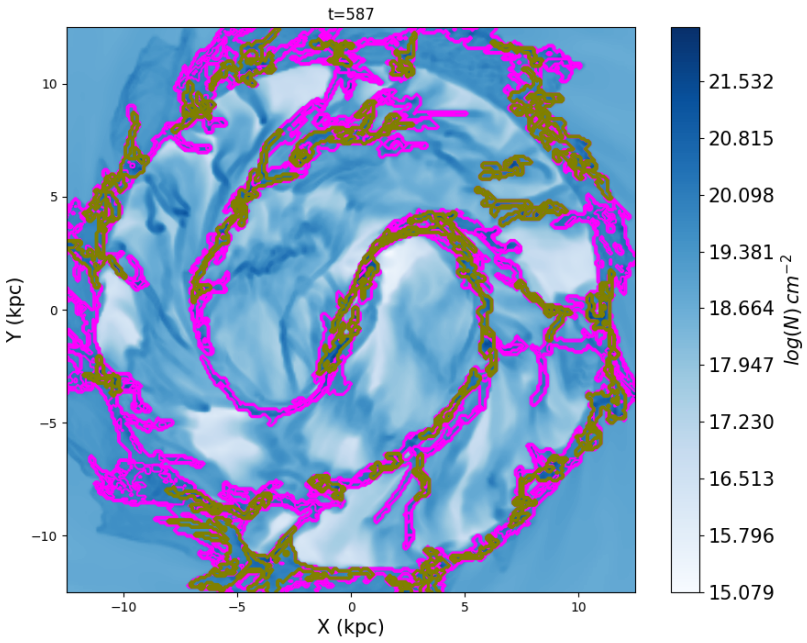


Figure 2.4: Density contour plot of the galaxy at evolution time of 587 Myrs, applying Astrodendro. Trunks are represented by magenta contours and leaves by olive color.

cell is below a density threshold it is removed because the purpose is to identify the highest density regions.

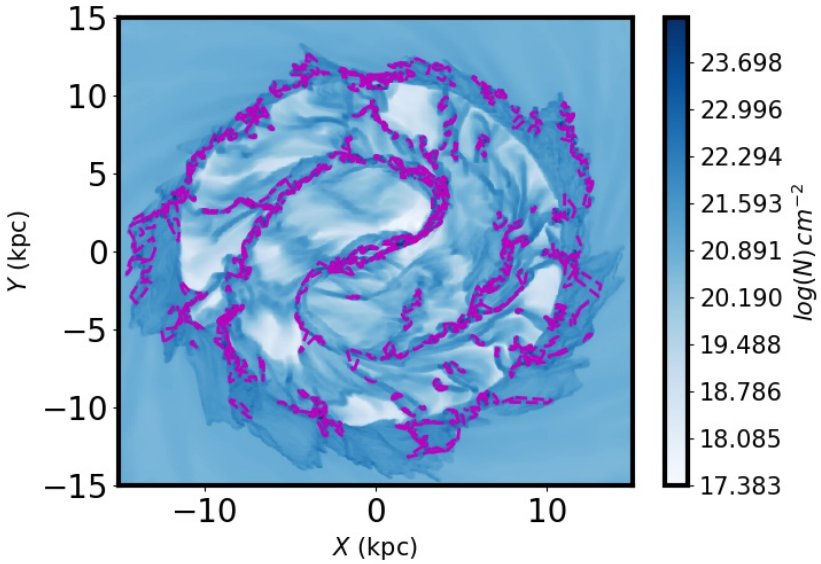


Figure 2.5: Density contour plot of the galaxy at evolution time of 587 Myrs, applying HOP algorithm.

Figure 2.5 shows the clouds that have been found by HOP algorithm as magenta contours.

A first visual approach for the three plots of ClumpFind and HOP, is that HOP finds smaller cloud structures than ClumpFind and this occurs probably because HOP acts directly on AMR grid.

### 2.1.8 Computing Cloud properties

Having identified the molecular clouds, we calculated some statistical properties for models MHD and HYDRO. We used the values of the code variables in each cell pertaining to a cloud in order to calculate its properties. These properties are mass with galactocentric radius, velocity dispersion with galactocentric radius, virial parameter with mass, velocity dispersion with mass, mass with radius and virial parameter with galactocentric distance.

For the calculation of cloud's radius, we used the third root of the cloud's volume.

We computed *virial parameter* using the following relation:

$$\alpha = \frac{5}{3}\frac{\sigma^2 R_{cloud}}{GM} \tag{2.11}$$

where $R_{cloud}$ is the cloud radius, G is the gravitational constant and M the mass of the cloud expressed in solar masses.

# Chapter 3

# Results

## 3.1 Galaxy simulation

An overview of the galaxy is presented in Figure 3.1 which shows the contour plots of total hydrogen column density on the x-y plane for the two models of Milky Way like galaxy, at evolution time of 1019 Myrs. Both panels show the galaxy in a radius of 20 kpc. Comparing the two models we notice that the distribution of the gas is different in two models. With a simple visual inspection, we see from Figure 3.1 that model *MHD* has more dense gas than model *HYDRO*.

## 3.2 Dense Gas

In order to investigate this difference in more detail, we calculated the mass of the dense gas of the clouds as a function of time. Figure 3.2 shows the mass of the dense gas versus time, between model *MHD* and model *HYDRO*. The solid lines show the absolute values and the dashed lines the differences between the two models. As we can see, for both models, from 0 to 250 Myrs the slope of the curve grows smoothly till the peak of the curve at about 500 Myrs. After that time, the dense gas increases in a similar way for both models.

As far as the differences between the two models are concerned, the dashed lines show that model *MHD* forms more dense gas from, approximately 200 to 800 Myrs. Then, both models have similar production of dense gas till 1250 Myrs. Except from 1600 Myrs, model *MHD* prevails model *HYDRO* for later times. This confirms the observation made in Figure 3.1.

It is interesting to investigate the reason why the magnetised model forms more dense gas. Might the magnetic field is linked to the star formation process.

In order to further investigate the role of the magnetic field in the star formation process in the molecular clouds, we calculated the mass in young stars for the two models. Figure 3.3 shows the mass in stars that do not belong

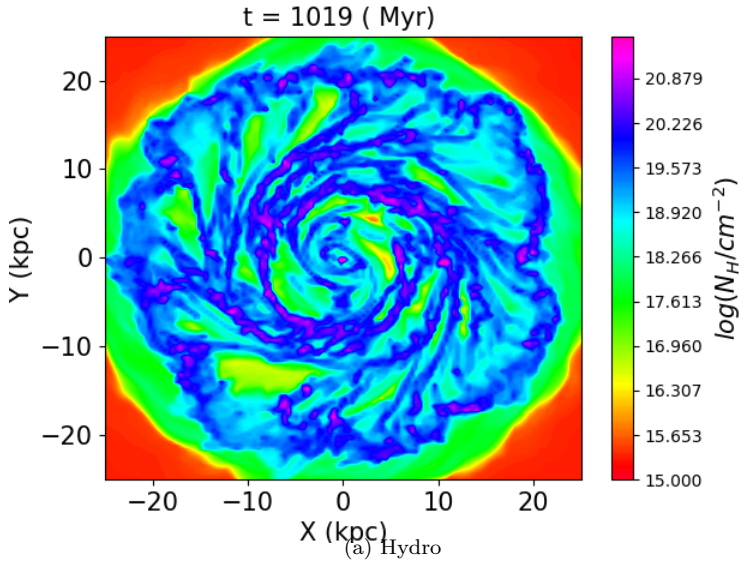


(a) Hydro

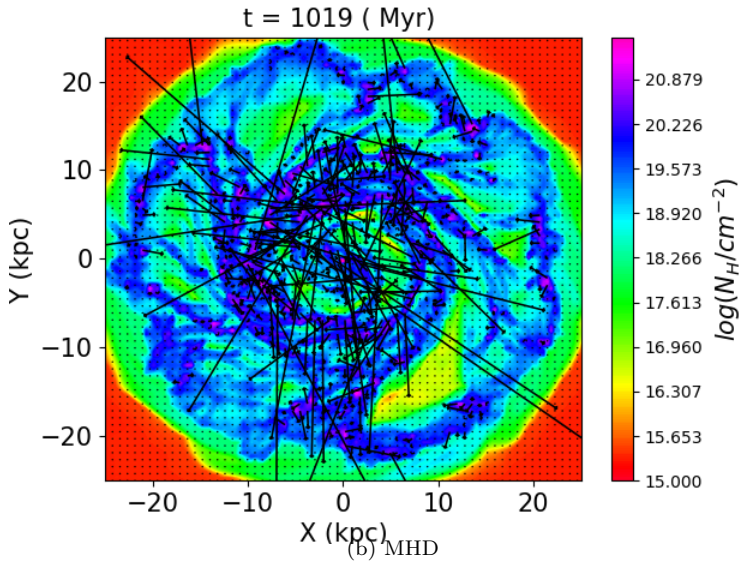


(b) MHD

Figure 3.1: The Milky Way like galaxy at evolution time of 1019 Myrs. The left figure is model *HYDRO* and the right one is model *MHD*.

to the initial distribution of stars, as a function of time between model *MHD* and *HYDRO*.

We see that the mass in young stars increases strongly after 500 Myrs, in model *MHD*. Also, at 500 Myrs, is the peak of the formation of dense gas

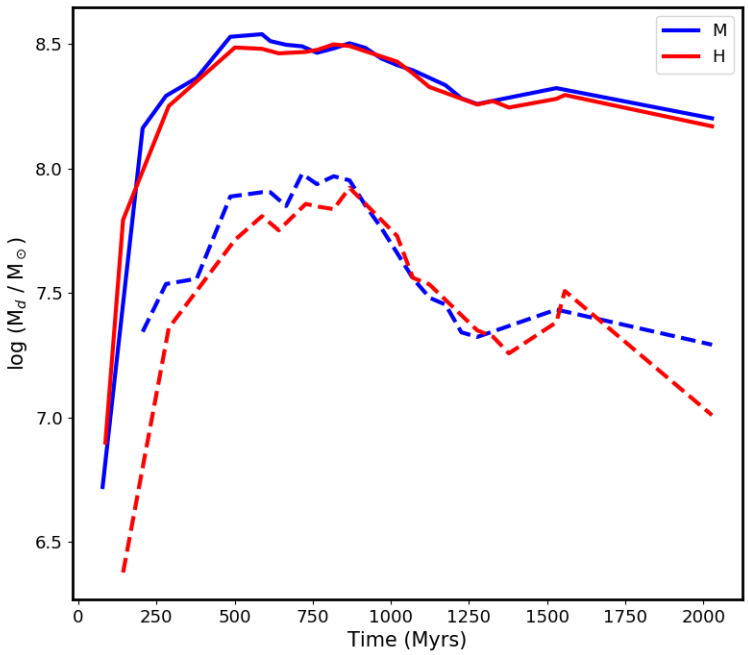


Figure 3.2: Dense gas as a function of time between model *HYDRO*, indicated as H and model *MHD* idicated as M.

according to Figure 3.2. To conclude, model *MHD* has more massive clouds than model *HYDRO* and this difference is amplified as the time passes.

This result is confirmed by Figure 3.4 that shows the number of young stars as a function of time, between the two models. Clearly the number of young stars is higher in model *MHD* than in model *HYDRO*. This difference is amplified as the galaxy evolves in time.

## 3.3 Star Formation Rate differences between the magnetised and the unmagnetised model

We found differences in two models in dense gas formation. As we saw in the Introduction, dense gas regions are stellar nurseries. So, does the magnetic field affect the star formation rate? And if it does, in what way and why?

We calculated the Star Formation Rate (SFR) for the two models as a function of time.

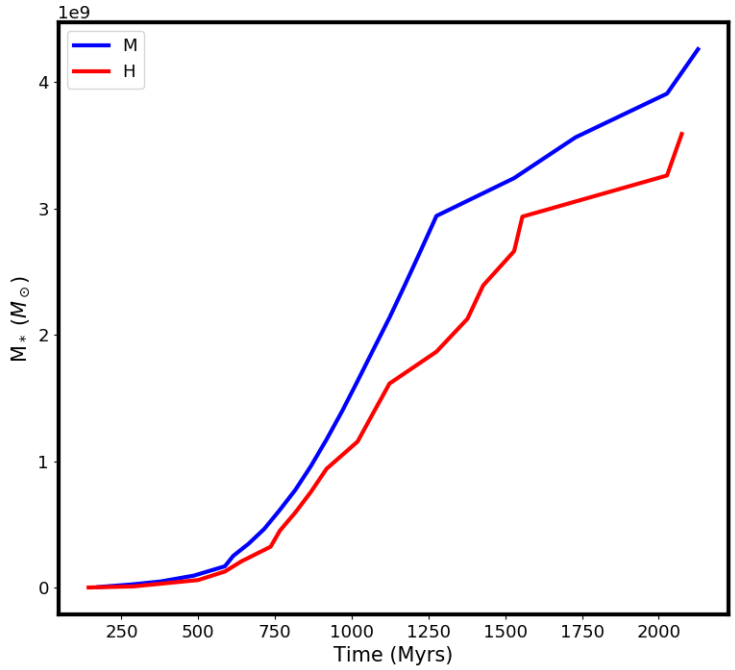


Figure 3.3: Mass in young stars as a function of time. The blue line corresponds to model *MHD* and the red line to model *HYDRO*.

$$SFR = \frac{M_*}{\Delta t} \tag{3.1}$$

Here, the SFR is defined as the mass of newly-formed stars in an interval $\Delta t$, here defined as the time interval between two consecutive snapshots, divided by $\Delta t$.

Figure 3.5 shows the SFR for the two models as a function of time. The most robust difference between the two curves happens at 500 Myrs. Also, at this time model *MHD* has a local maximum in SFR. It's total maximum is at 750 Myrs while model *HYDRO* prevails, but not so intensely like at 500 Myr. At later times the SFR differences between the two models are more smooth.

## 3.4 Gas distribution as the galaxy evolves

As we saw, the dense gas formation in both models changes through time. But, does these changes accompany the whole gas distribution of the models? Does magnetic field affects the gas distribution and therefore the star formation

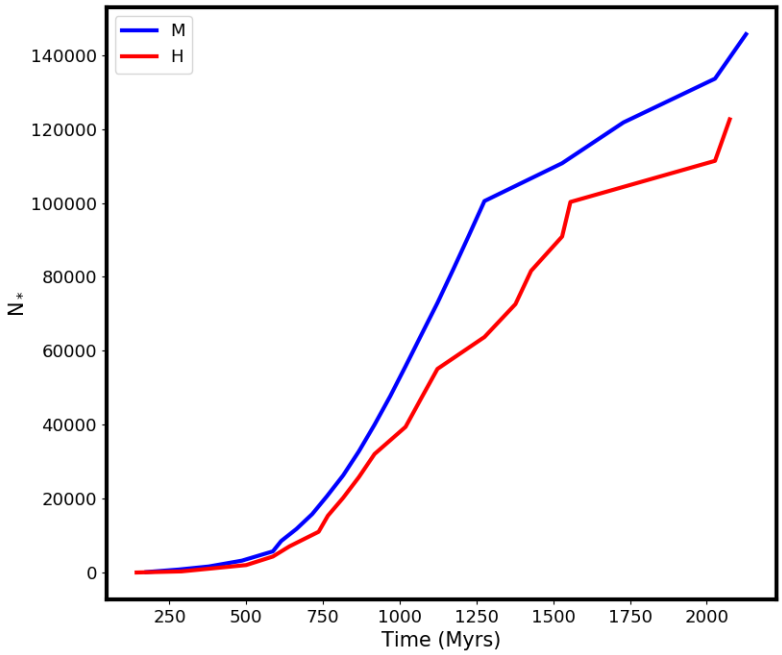


Figure 3.4: Number of young stars as a function of time between model *MHD* (M) and model *HYDRO* (H).

process? So, in order to understand the role of magnetic field in star formation, we studied the gas distributions of both models at different times.

The distribution of the gas is presented by contour plots of total hydrogen column density on the x-y plane of the central region. We compare MHD and HYDRO in zoomed-in regions in order to have a better overview. The radius of the zoomed-in region is 4 kpc.

Figure 3.6 shows the two galaxies at evolution time of 587 Myr. The vectors in *MHD* model are not normalised so we can see both the intensity and the direction of the field. From the vector field we can see that the magnetic field is more intense mostly at the densest regions. The other interesting thing is that a nuclear bar is forming. Finally, we notice that the great intensity of the field follows the form of the bar. This is a signature of the initial condition, which starts off much stronger in the central regions of the galaxy.

Figure 3.7 is similar to Figure 3.6 but at 867 Myr. In this 4 kpc region, we observe some clouds in the central region that did not exist at Figure 3.6 . Comparing *HYDRO* and *MHD* we can clearly see that the cloud in *HYDRO* located in 1.3 kpc, seems to be elongated in *MHD*. Also, the magnetic field is more intense at higher density regions.

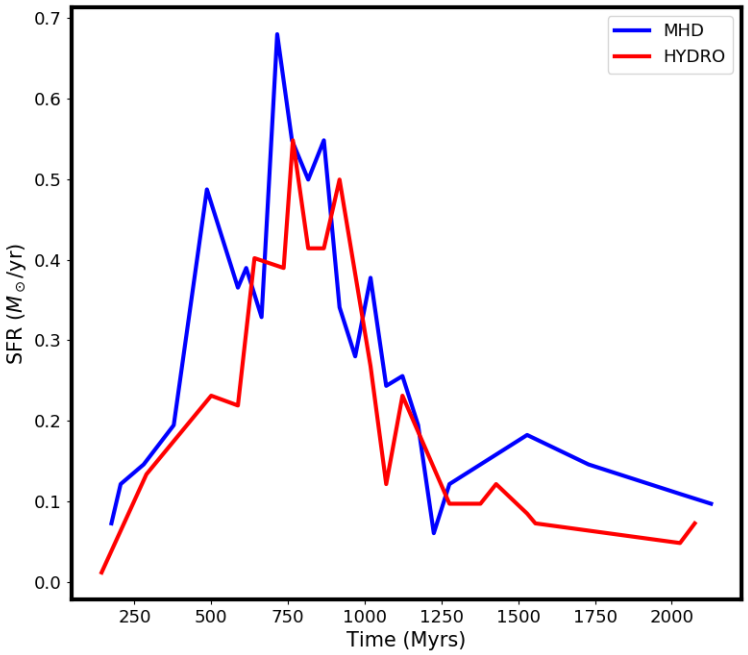


Figure 3.5: SFR as a function of time. The blue line corresponds to the galaxy with magnetic field (*MHD*) and the red to the one without (*HYDRO*).

In the central region of Figure 3.8 in the *MHD* run the filaments have greater density and seems to be wound up by rotation. The magnetic field intensity follows the same tendency as the previous times.

The density of the filaments in Figure 3.9 is higher. Also, there is a phase difference between the two models, as the central bar seems to have rotated a few degrees further in model MHD comparing the two snapshots.

The central region of Figure 3.10 shows a growing phase difference in the rotation of the two models. Moreover, the nuclear bar has a different length between the two models, with the one in *MHD* being larger and thinner.

In conclusion, comparing the five snapshots, we can see that the distribution of the gas changes as the galaxy evolves. Gradually, the formation of a nuclear bar is present in both models. But, from the contour plot it appears the the nuclear-bar region forms more dense gas in model *MHD* than in model *HYDRO*. Relating the star formation to dense gas, this result agrees with the finding that the SFR in model *MHD* is, on average, higher.

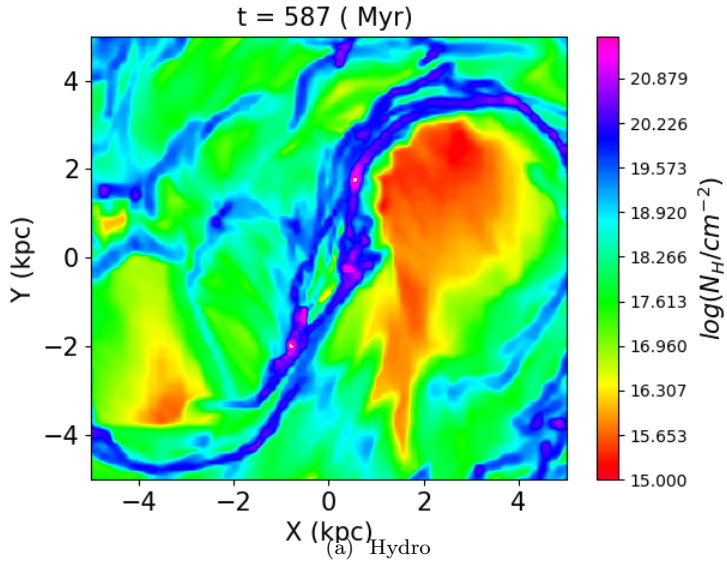


(a) Hydro

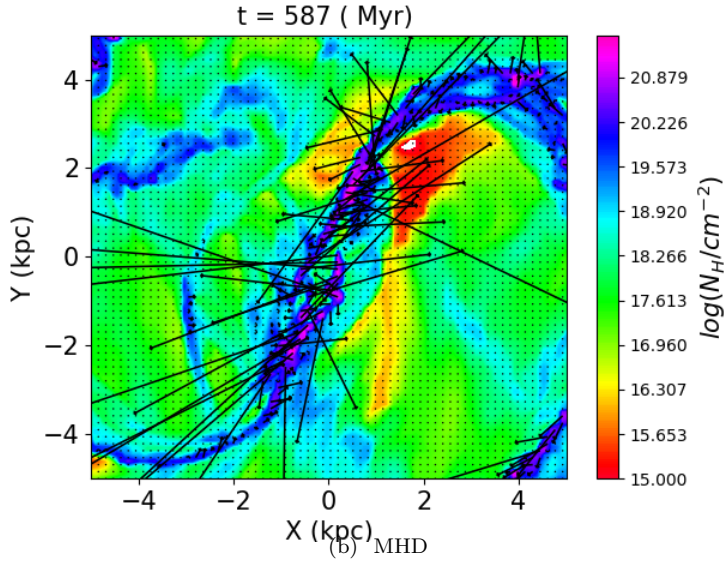


(b) MHD

Figure 3.6: The mass- weighted contour plot of total hydrogen column density on the x-y plane for the two models. Specifically, the center of the galaxy on 587 Myr and spatial scale of 4 kpc. The black arrows show the projected magnetic field. The vectors are not normalised.

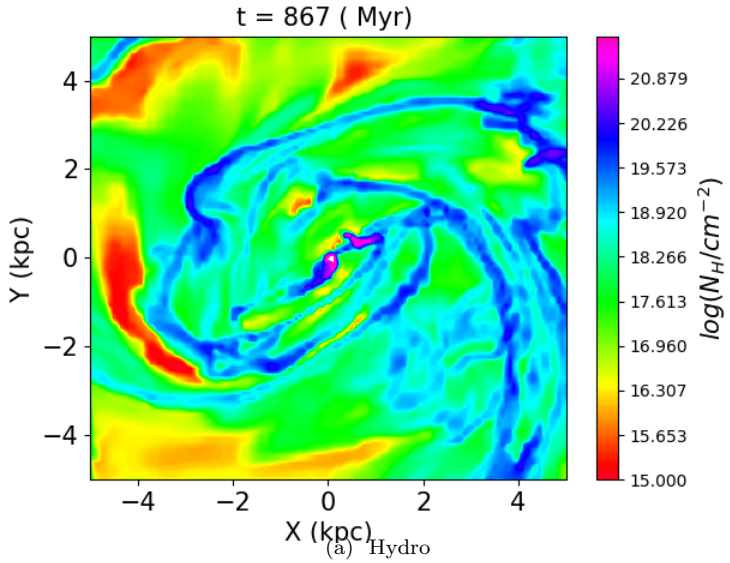


(a) Hydro

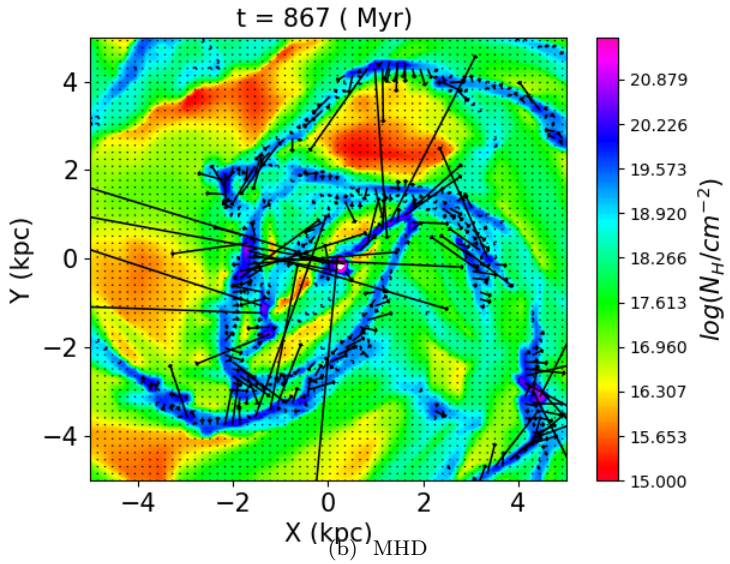


(b) MHD

Figure 3.7: Similar to Fig.1.

## 3.5 Cloud positions and properties

In order to further investigate the properties of the star-forming gas, we identified the dense clouds and calculated some of their properties looking for potential differences between the two models.

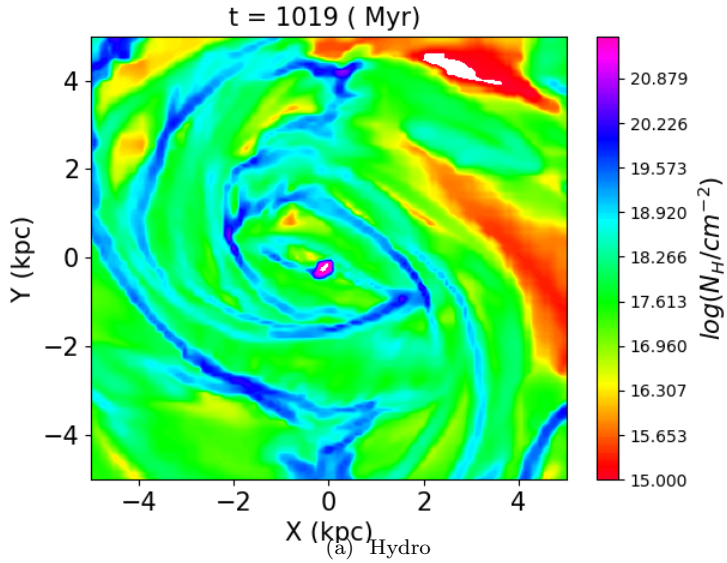


(a) Hydro

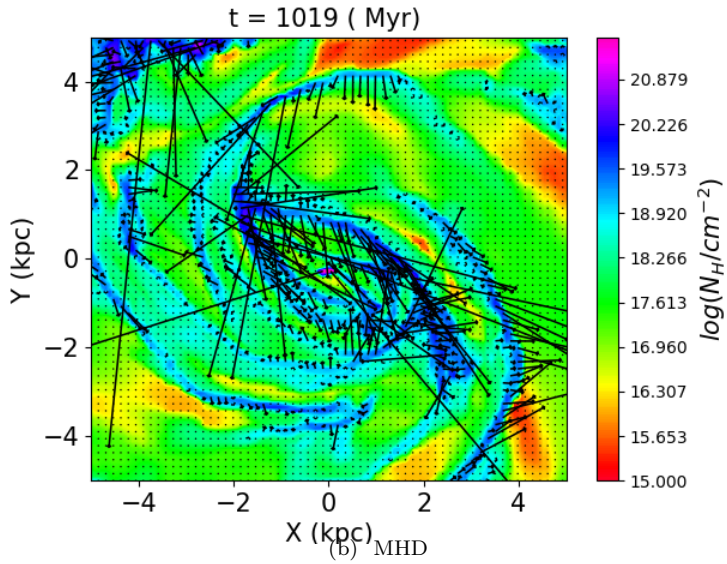


(b) MHD

Figure 3.8: Similar to Fig 1.

### 3.5.1 Cloud Identification

To investigate the cloud locations, we used the dendrogram algorithm to locate the cloud positions, indicated by contours. The contours were applied on dendrogram's leaves. Figures 3.11, 3.12, and 3.13 show the cloud locations at

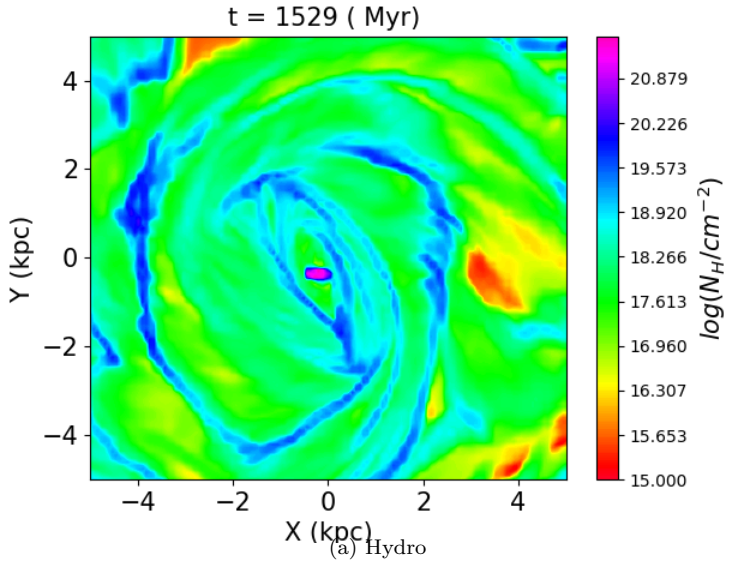


(a) Hydro

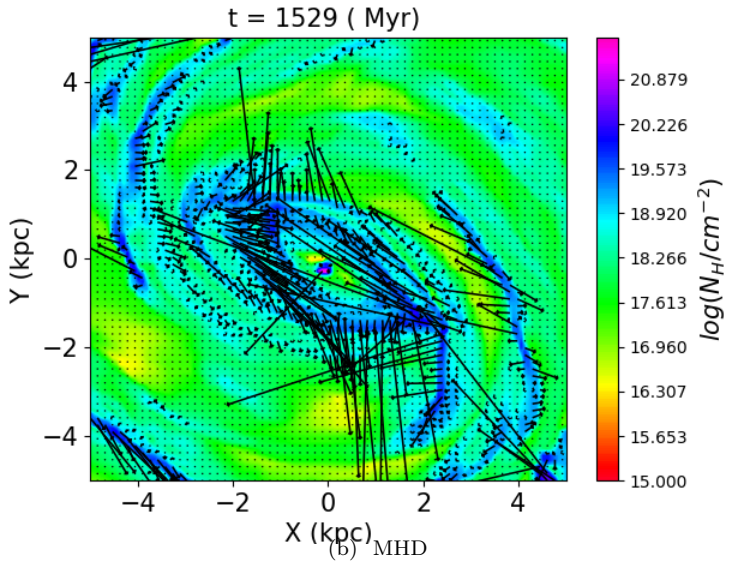


(b) MHD

Figure 3.9: Similar to Fig.1.

three different resolutions and in time 2027 Myrs. In order to investigate the molecular clouds in more detail, we interpolate the AMR data on a uniform grid of gradually higher resolution. This is done because the dendrogram implementation that we used needs data in equal-sized cells. However, it does not require the data cube to be of equal size in three dimensions, so we choose an

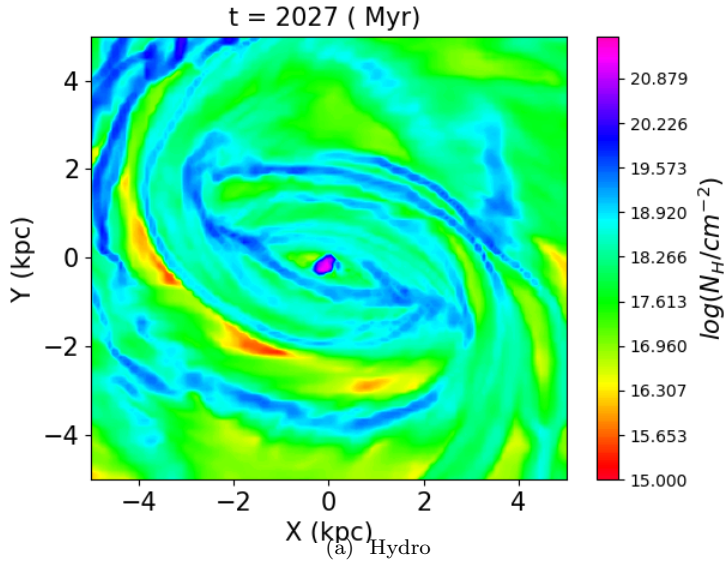


(a) Hydro

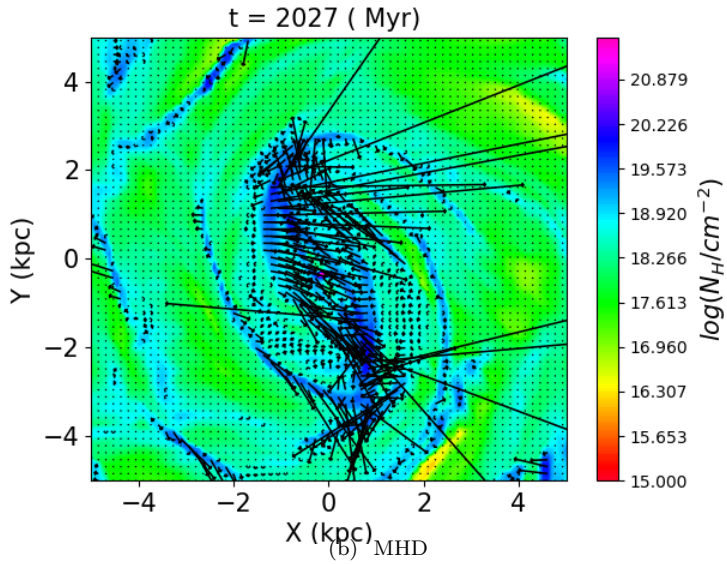


(b) MHD

Figure 3.10: Similar to Fig.1.

aspect ratio of $y/x = 1$, but $z/x = 0.125$. This allows us to select the entire disk and still have arrays of computationally manageable size. As we will see in the following, this is not true of the Clumpfind implementation, which requires as input a cube with equal resolution in each side.

From Figure 3.11 we can see that, at a resolution of $1024^3$, the algorithm

does not only find dense clouds in the region of the nuclear bar but also identifies the ones at the edge of the galaxy in the spiral arms. Also, the algorithm finds less clouds in model *MHD* compared to *HYDRO*.

Figure 3.12 shows a snapshot with higher resolution than Figure 3.11. At this resolution the algorithm finds more clouds not only in the central region but also in total. Again, less clouds of model *MHD* have been identified.

Moving to the third and highest resolution (3.13), we can see that as a whole, the algorithm finds more clouds than at lower grid resolution. This observation is not surprising because with higher resolution we have access to more substructure. Our observation is consistent with the recent findings of Louvet et al. (2021), who showed that, both in simulations and observations of molecular clumps, increasing the resolution led to smaller and less massive substructure. In general, this lack of convergence is a standing problem in the study of molecular clouds.

To confirm this behavior with resolution, we made a mass histogram of the clouds at different resolutions (Figure 3.14). As a reminder, resolutions of $2^{10}$,$2^{11}$ and $2^{12}$ correspond to 1024, 2048 and 4096 cells in each direction. These plots reveal the discrepancies that emerge by changing the resolution. The blue line shows the mass of the clouds at resolution of $2^{10}$, the red line corresponds to resolution of $2^{11}$ and the green line to $2^{12}$. Clearly, the lower resolution corresponds also to the least number of clouds, and that agrees with the observations from Figure 3.11.

Due to the resolution issues that emerge and to avoid interpolation, we used HOP algorithm, which identifies the molecular clouds directly from the AMR grid. The HOP implementation for RAMSES data was kindly provided by Patrick Hennebelle.

### 3.5.2 Cloud properties

After the GMCs identification process from the different algorithms we came to a conclusion that ClumpFind and Dendrogram rely on resolution. Specifically, when we increased the resolution with Dendrogram the algorithm was finding more GMCs. Similar behavior appears with the use of ClumpFind. Despite the resolution issues, used the GMCs identified by Dendrogram and calculated some statistical properties. Then, we applied ClumpFind and did the same. Finally we calculated the properties of the clouds identified by HOP. The reason for using all the different algorithms is to investigate if the properties of the GMCs are affected by resolution issues or depend on the algorithm. And finally if there are any differences between the two models and which algorithm exposes such differences.

#### Results from Dendrogram

After picking a resolution of 1024 cells per direction ($2^{10}$), we calculated some statistical properties of the clouds idntified by the Dendrogram algorithm.

Figure 3.15 shows the mass of the clouds as a function of their distance from the galactic center. At both snapshots we observe the same distribution for both models.

Figure 3.16 shows the velocity dispersion of the clouds as a function of galactocentric distance. We observe that around a radius of approximately 1 kpc, both models in both snapshots have the same range in the distribution values.

Figure 3.17 shows the virial parameter of the cloud as a function of its mass. Both snapshots are almost the same. Also, there are no great differences between the two models. Furthermore, we observe from the Figure that the distribution is near the value of $-0.5$ while the value of $log20.3$ indicates the stability of the cloud. So, there are both stable and unstable clouds.

Figure 3.18 shows the velocity dispersion of the cloud as a function of its mass. The two snapshots show the same distribution whereas there is no difference between the two models.

Figure 3.19 shows the radius of the cloud as a function of its mass. Again, there are no great differences between the snapshots and the models.

### Results from ClumpFind

As a compromise to facilitate the computation, we have chosen to work with a resolution of 1024 cells per direction ($2^{10}$) for the PyCupid package computations. The clouds were identified by ClumpFind , as explained in the previous chapter. Figures 3.20, 3.21, 3.22 show properties of clouds found by ClumpFind. The blue symbols correspond to model *HYDRO* and the red ones to model *MHD*.

Figure 3.20 shows the cloud internal velocity dispersion as a function of mass. At all times, the two models have almost the same distribution. Also, this property is compatible with Larson's relation (Eq.1.3).

In Figure 3.21 we plot the mass of a cloud in solar masses as a function of its radius. The general tendency for both models is that they follow the same distribution among similar value range.

Another property that we studied is the mass of the cloud as a function of the galactocentric distance in order to investigate if there is a tendency for the clouds to be more massive in the center as we have noticed from the contour plots. However, taking a look in Figure 3.22 we find no such tendency.

We conclude that the properties of molecular clouds in the two models do not show great differences. Nevertheless, as Figure 3.5 shows, the magnetised model forms more stars than the un-magnetised. For this reason, we calculated the total mass contained in the clouds of each model using ClumpFind.

Figure 3.23 shows histograms of the total mass. At 1019 Myrs *MHD* has greater total mass in clouds than model *HYDRO*. On the contrary, at 1529 Myrs, model *HYDRO* has got greater total mass.

To confirm that statement, we calculated total masses with time with ClumpFind. Figure 3.24 shows the mass in clouds as a function of time for model *MHD* and *HYDRO*. Apart from 1019 Myr, model *HYDRO* has higher total mass with a peak in approximately 500 Myrs. But, comparing with Figure 3.2 these two

figures come into juxtaposition. The reason is that Clumpfind accepts some configuration parameters in order to process the given input, in this case a density array. For this reason it excludes some percentage of the dense gas. On the contrary, Figure 3.2 was made directly by the simulation so it is more valid than Figure 3.24.

To sum up, we find that model *MHD* makes more massive clouds and has a higher SFR. The difference in total mass of the clouds might be an indicator that the magnetic field shapes the dense gas in a way that the ideal conditions are created for collapse.

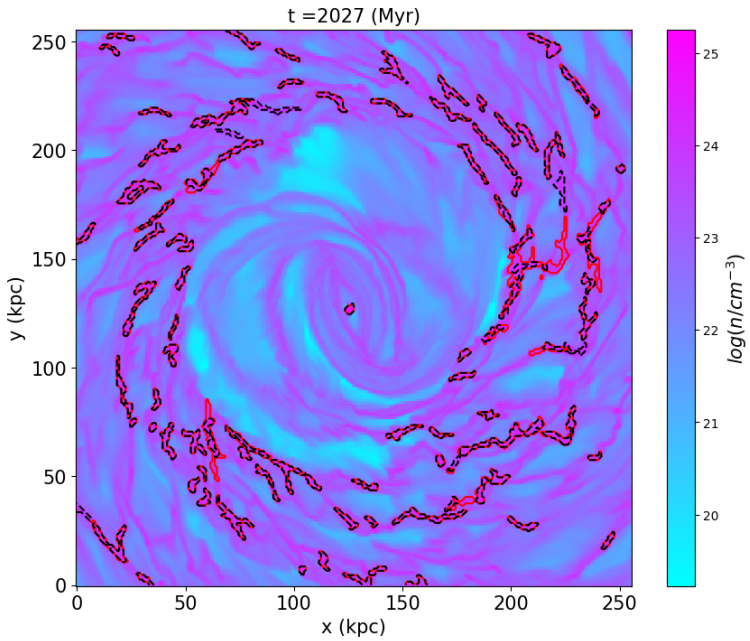


(a) Hydro

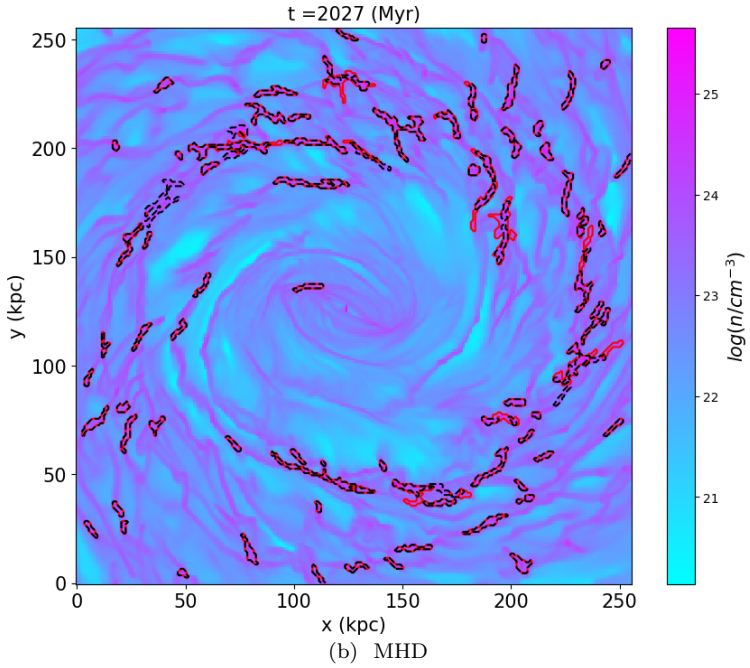


(b) MHD

Figure 3.11: Contour plot of the galaxy at resolution of 1024 cells per direction. The black colored contours indicate the location of the clouds found by dendrogram.

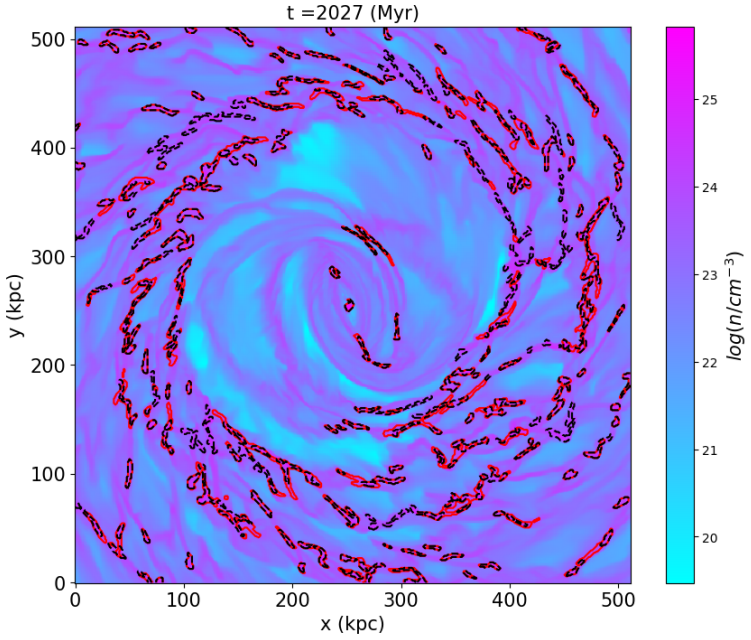


(a) Hydro

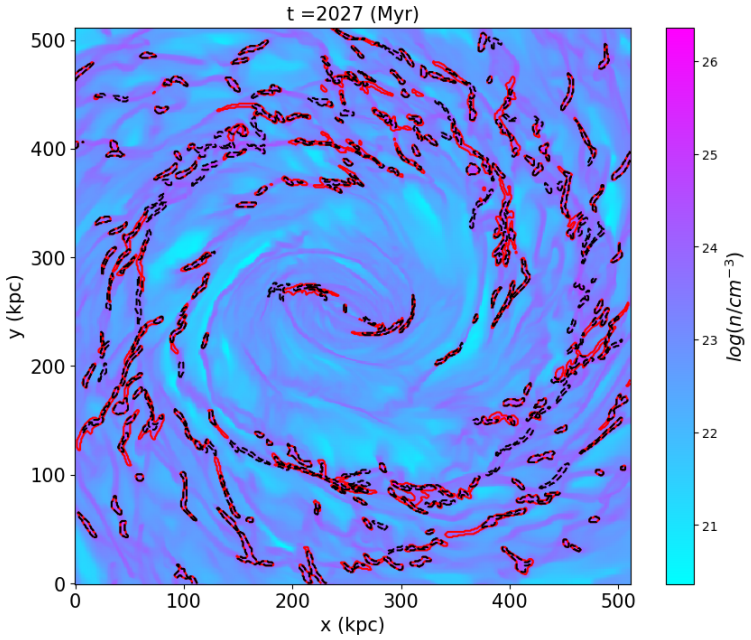


(b) MHD

Figure 3.12: Contour plot of the galaxy at resolution of 2048 cells per direction. The black colored contours indicate the location of the clouds found by dendrogram.

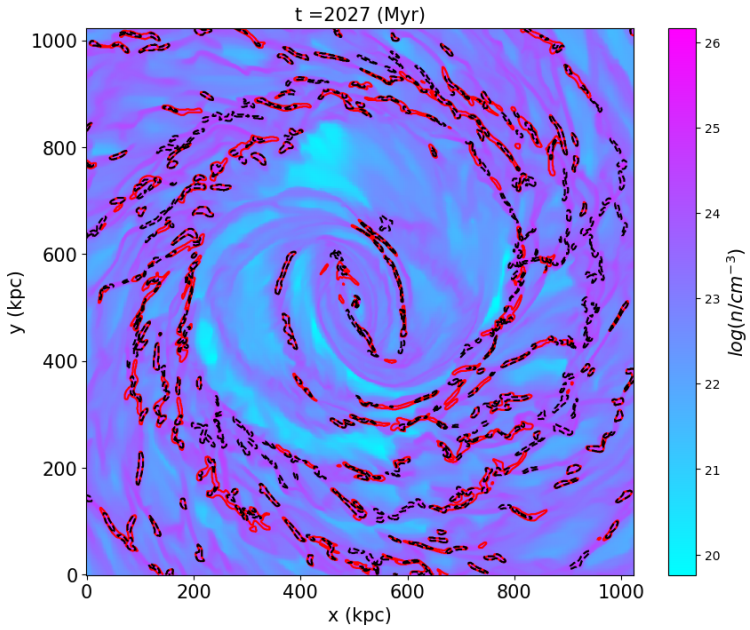


(a) Hydro

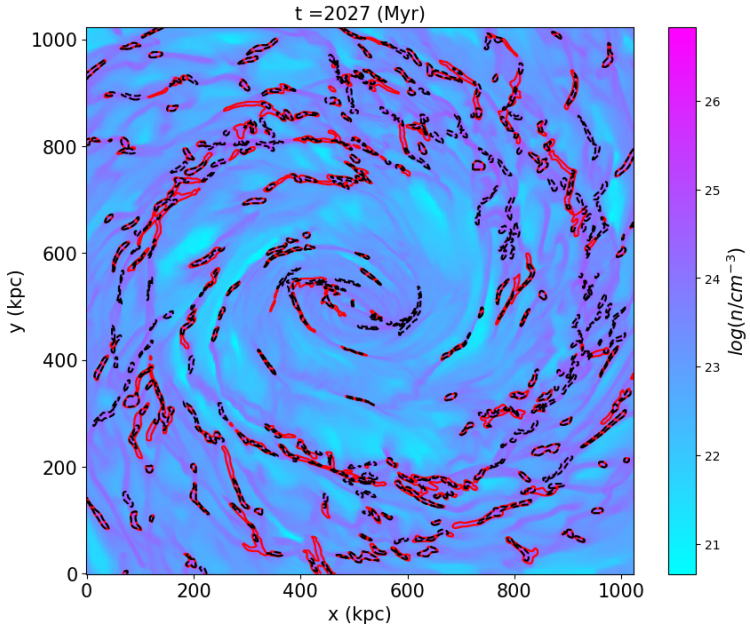


(b) MHD

Figure 3.13: Contour plot of the galaxy at resolution of 4096 cells per direction. The black colored contours indicate the location of the clouds found by dendrogram.

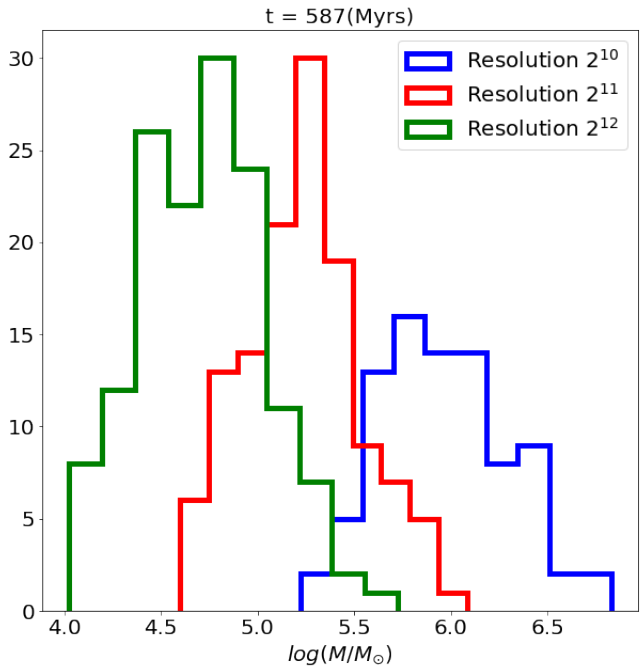


Figure 3.14: Mass histogram of resolutions of $2^{10}$, $2^{11}$ and $2^{12}$.

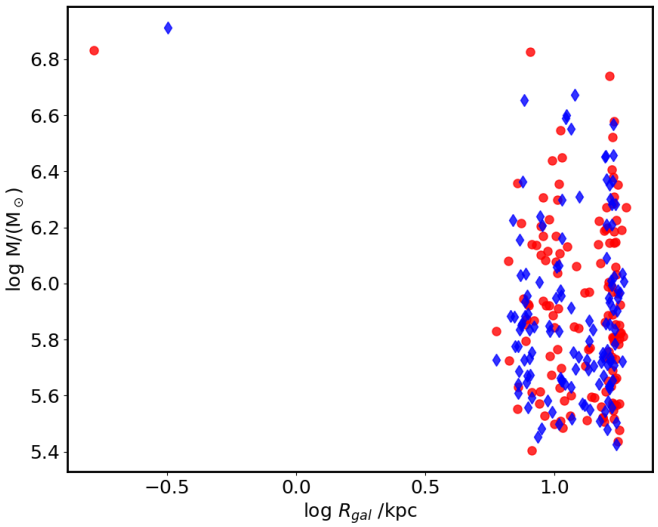


(a) t = 1529 Mys

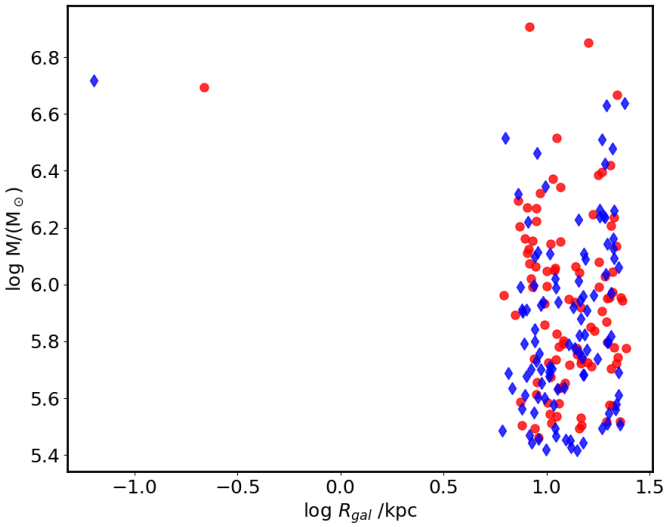


(b) t = 2027 Myrs

Figure 3.15: Mass as a function of galactocentric distance. The red points correspond to model MHD and the blue ones to model HYDRO. These properties were calculated using Dendrogram.

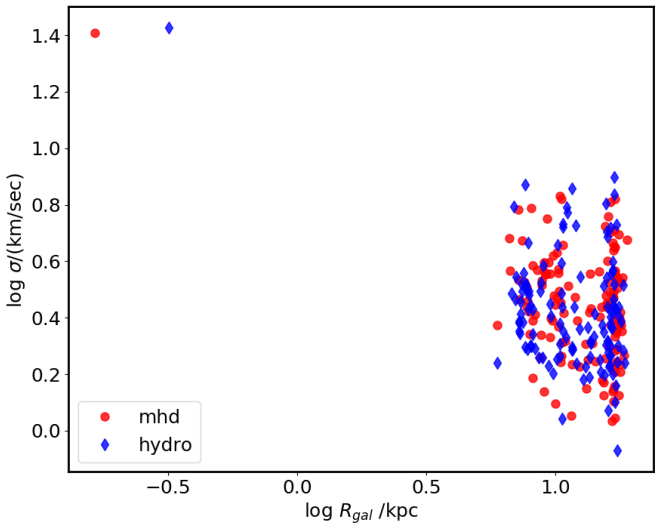


(a) t = 1529 Mys

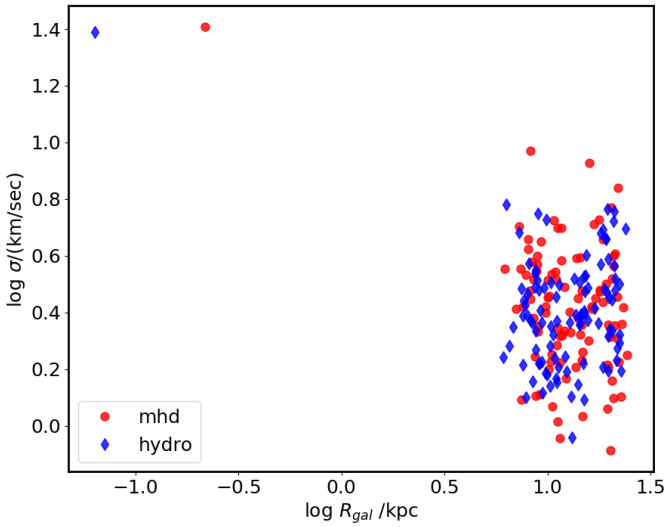


(b) t = 2027 Myrs

Figure 3.16: Velocity dispersion as a function of galactocentric distance. The red points correspond to model MHD and the blue ones to model HYDRO. These properties were calculated using Dendrogram.

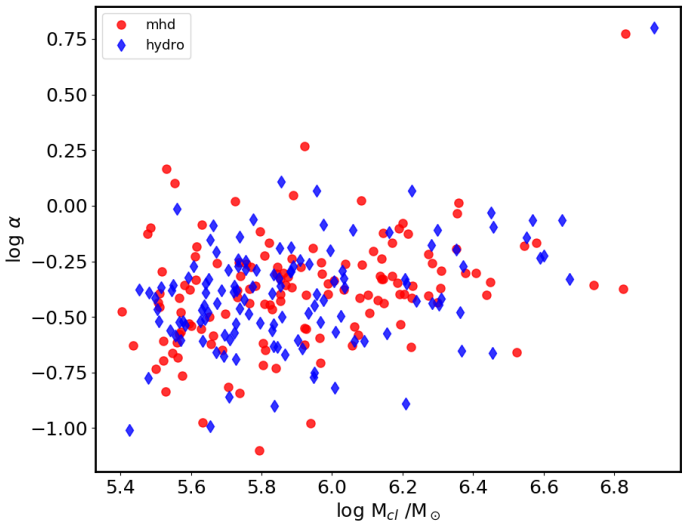


(a) t = 1529 Mys

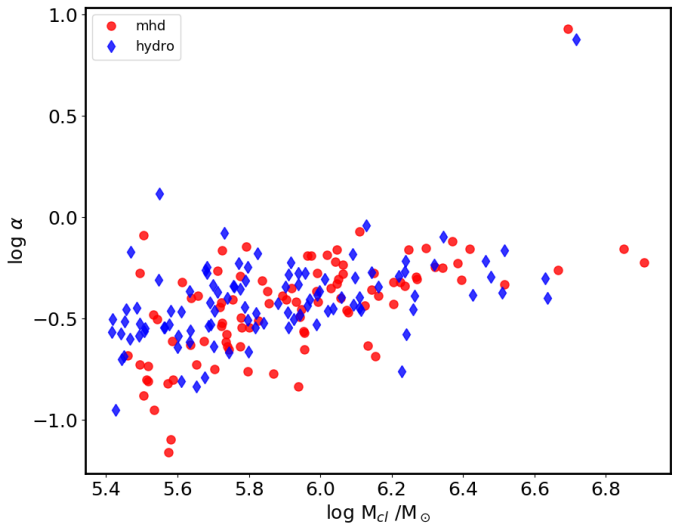


(b) t = 2027 Myrs

Figure 3.17: Virial parameter as a function of the clouds mass. The red points correspond to model MHD and the blue ones to model HYDRO. These properties were calculated using Dendrogram.

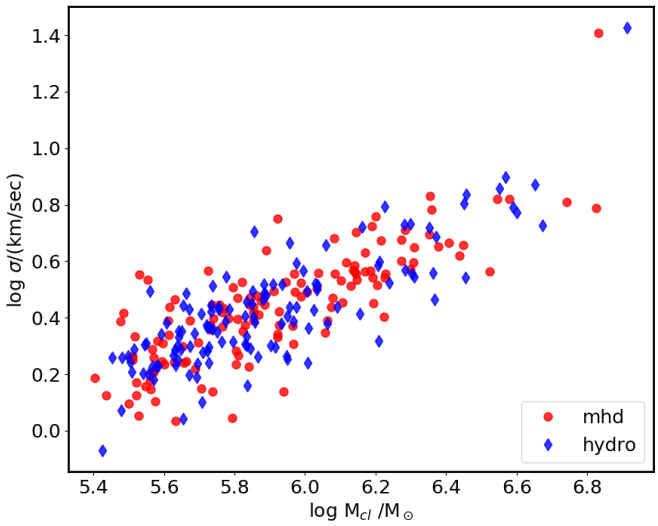


(a) t = 1529 Mys

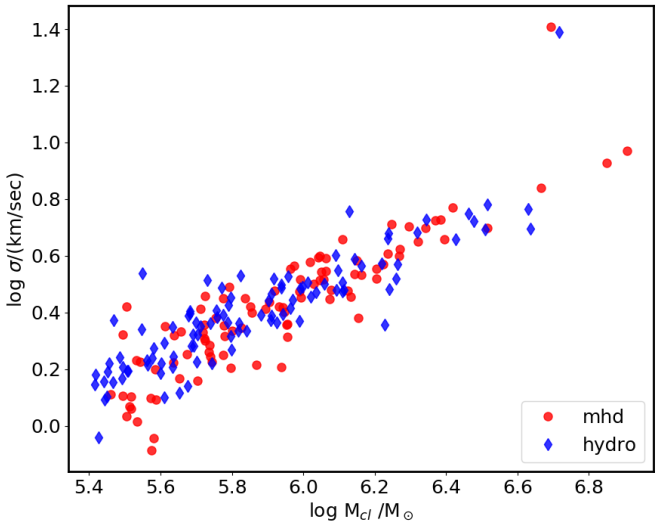


(b) t = 2027 Myrs

Figure 3.18: Velocity dispersion as a function of mass. The red points correspond to model MHD and the blue ones to model HYDRO. These properties were calculated using Dendrogram.

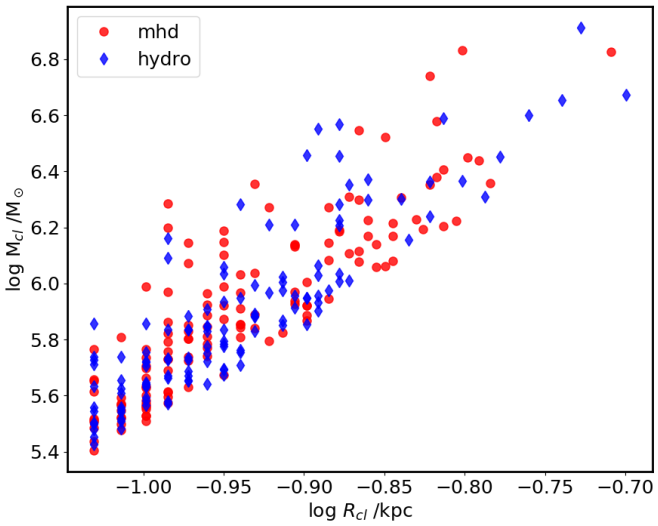


(a) t = 1529 Mys

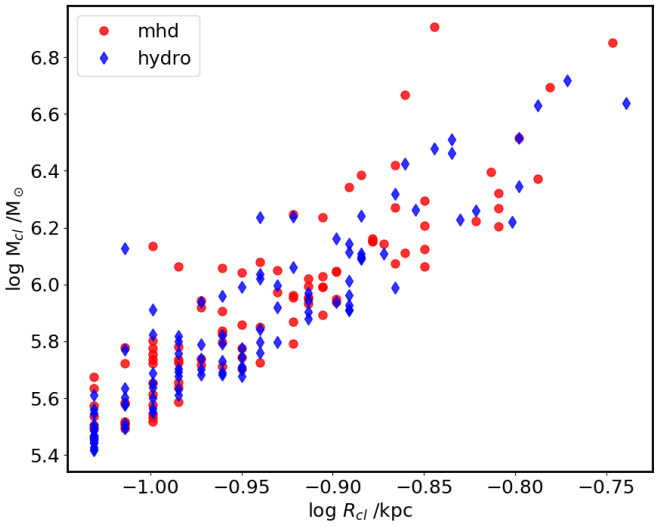


(b) t = 2027 Myrs

Figure 3.19: Cloud mass as a function of radius. The red points correspond to model MHD and the blue ones to model HYDRO. These properties were calculated using Dendrogram.

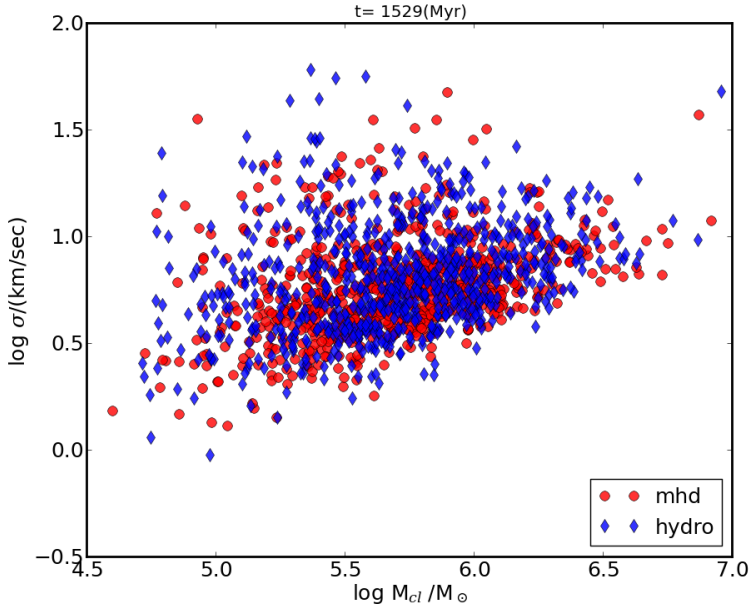


(a) ClumpFind

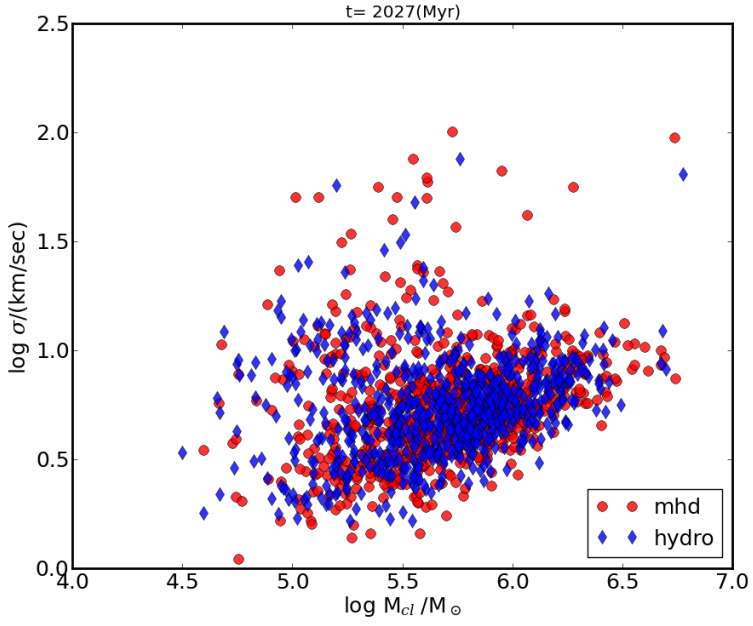


(b) ClumpFind

Figure 3.20: The logarithm of velocity dispersion $\sigma$ with the logarithm of the cloud mass in solar masses in different times :(a) 1529 Myr, (b) 2027 Myr The red dots represent the MHD model and the blue rhombi represent the HYDRO model.

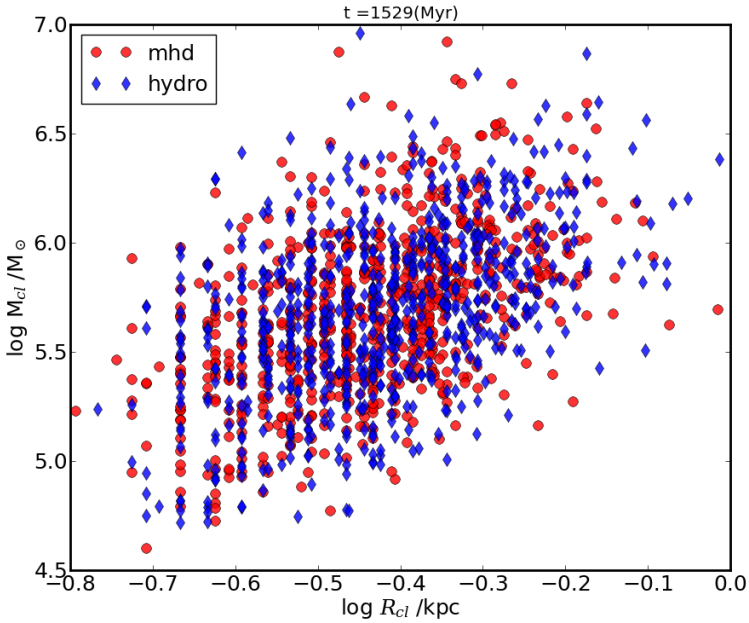


(a) ClumpFind

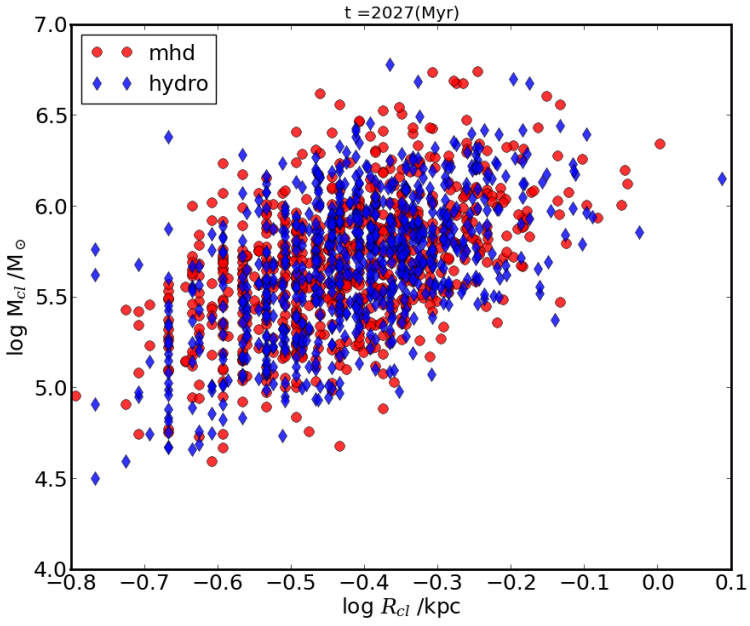


(b) ClumpFind

Figure 3.21: Mass with radius.

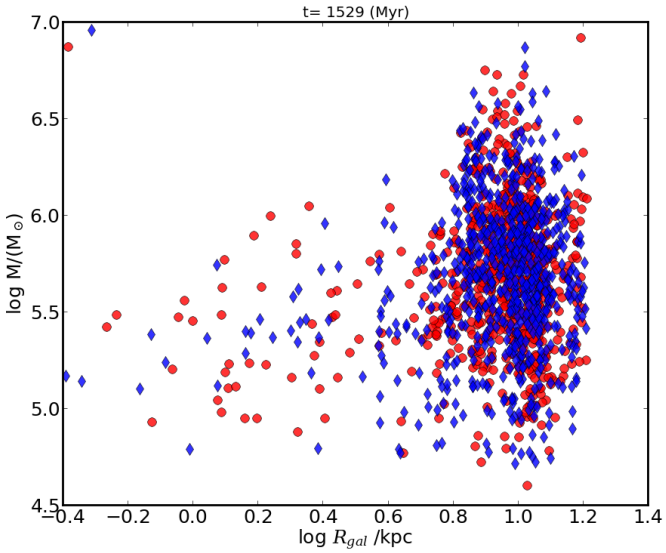


(a) ClumpFind

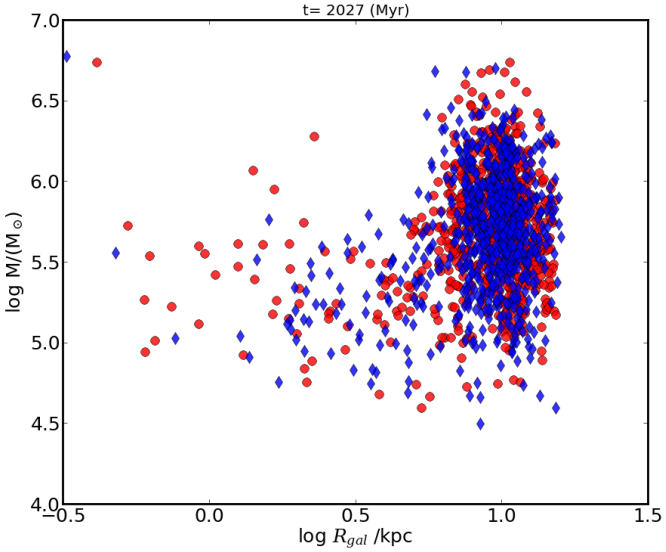


(b) ClumpFind

Figure 3.22: Mass as a function of galactocentric distance.

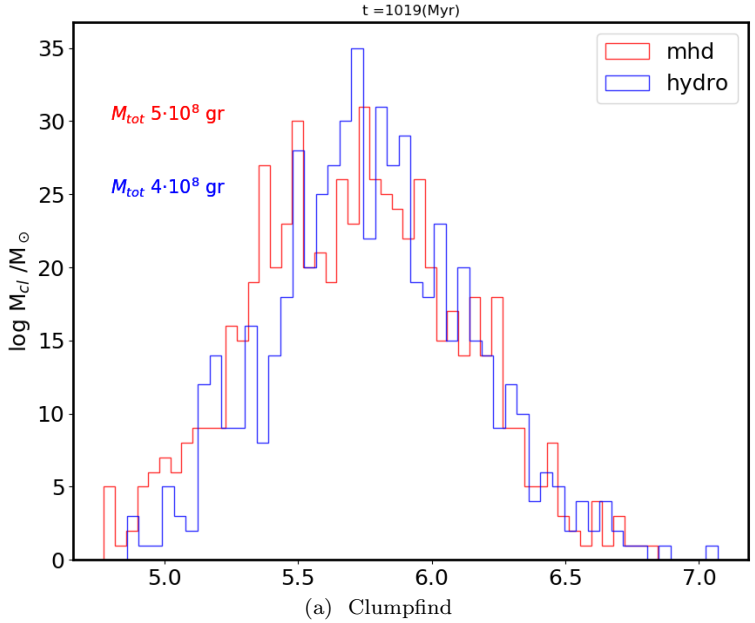


(a) Clumpfind

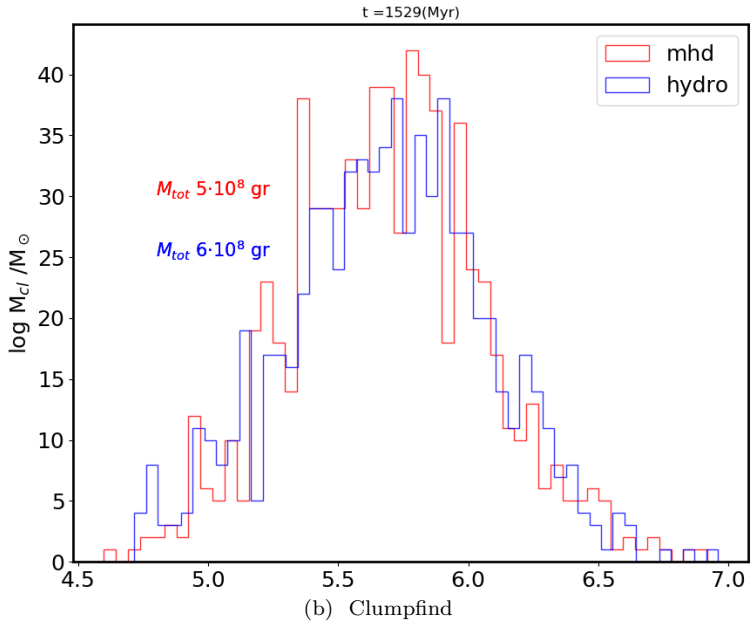


(b) Clumpfind

Figure 3.23: Histogram of total mass of molecular clouds in two models. The blue line represents model HYDRO and the red one, model MHD.

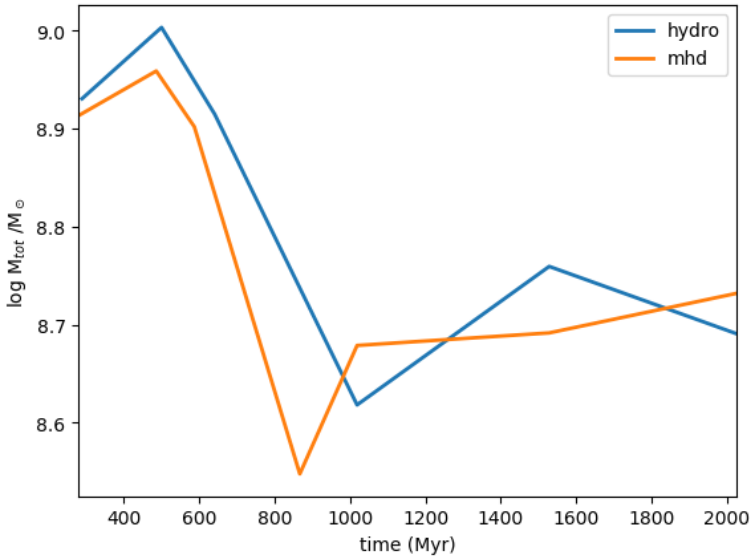


Figure 3.24: Total mass in molecular clouds as a function of time between two models by different algorithms. The blue line represents HYDRO and the red and orange, model MHD.

**Results from HOP**

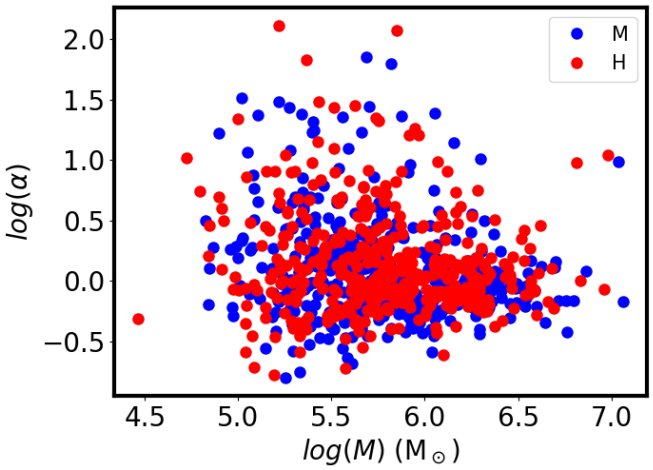


(a) t = 1529 Mys

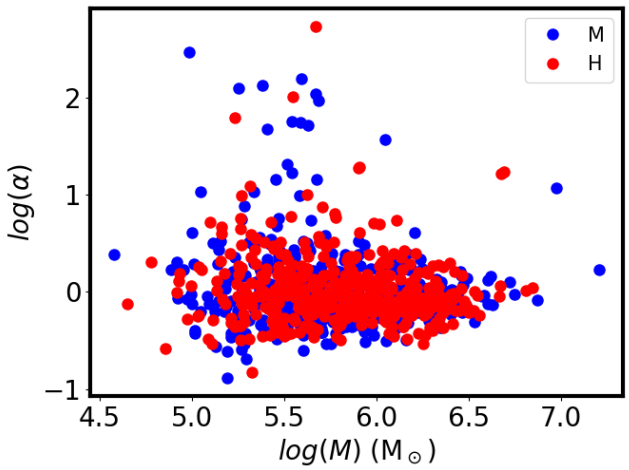


(b) t = 2027 Myrs

Figure 3.25: Virial parameter as a function of the cloud's mass in different evolution times. The blue points correspond to model MHD and the red ones to model HYDRO. The plot was created by using the HOP algorithm.

Figure 3.25 show the virial parameter of the cloud as a function of its mass.

For all the four snapshots we notice that the virial parameter is similar for both models and its value is around zero. Clouds that are below this value are considered stable against collapse.

Figure 3.26 shows the virial parameter of the cloud as a function of the distance from the galactic center. The two snapshots correspond to two different times. In particular, the times scales are 1529 and 2027 Myrs. The values are scattered around by the value 0.5 for the virial parameter. Finally, although we do not see any major differences between the two models, the distribution for the snapshots differs. However, this is expected because the distribution of the dense gas is different as we showed in the previous sections.

Figure 3.27 show the velocity dispersion of the cloud as a function of its mass. Although the scatter between the two snapshots differs, they do not have any great differences. Meanwhile, the two models are similar.

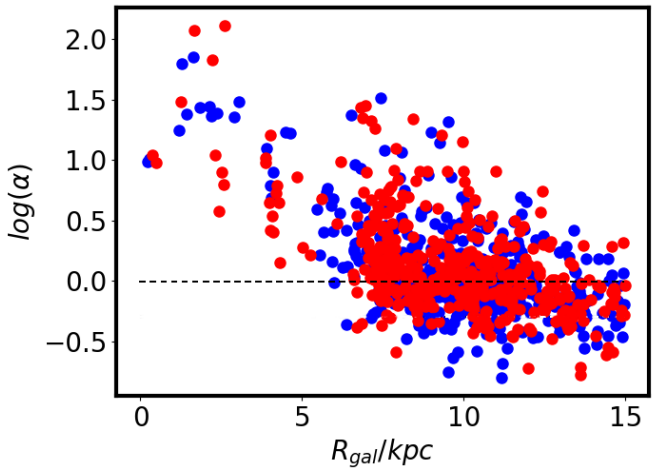


(a) t = 1529 Myrs

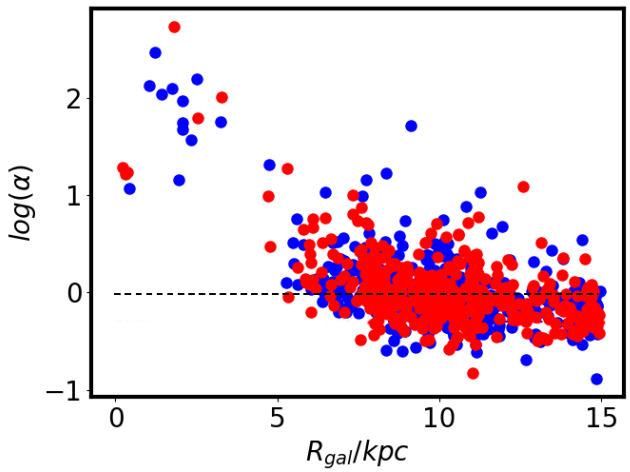


(b) t = 2027 Myrs

Figure 3.26: Virial parameter as a function of the cloud distance from the center of the galaxy, at different evolution times. The dashed line shows where $\alpha$=0.5.The blue points correspond to model MHD and the red ones to model HYDRO. The plot was created by using HOP algorithm.

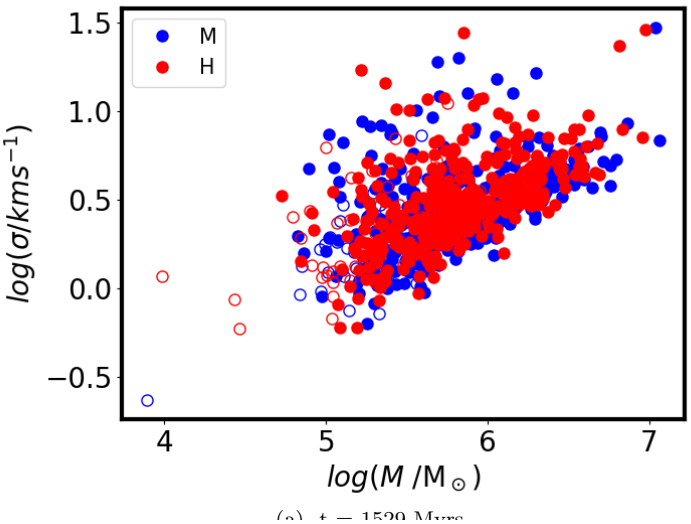


(a) t = 1529 Myrs

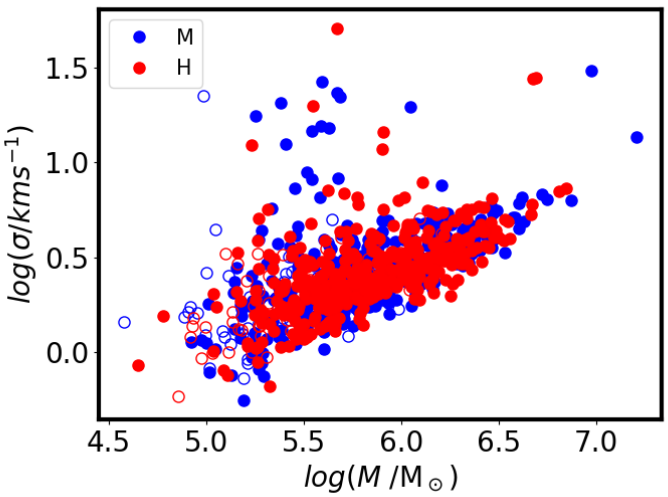


(b) t = 2027 Myrs

Figure 3.27: Velocity dispersion of the clouds as a function of their mass, at different evolution times.

# Chapter 4

# Summary and Discussion

In this work, we have investigated the possible effect of the magnetic field on the dense gas distribution and properties of two galaxy models simulated with the RAMSES code, as described in Ntormousi et al. (2020). The two models are identical, except that one model is magnetised (model MHD), while the other is not (model HYDRO).

We have compared the dense gas distribution and we found that the magnetised model forms more dense gas and has a higher SFR than the un-magnetised one by approximately 10%.

In order to find out the reason why this is happening, we turned to the molecular clouds and their properties. The first step was to identify those clouds. For this purpose, we used three different algorithms, Dendrogram, Clumpfind and HOP. We concluded that the implementation of the first two algorithms relies on resolution. In particular the lower the resolution is the less clouds are identified. For this reason we turned to the third, for which we have access to an implementation that acts directly on the AMR grid. Meanwhile, we used all the algorithms to calculate the statistical properties. With Dendrogram we examined the following properties: mass with galactocentric radius, velocity dispersion with galactocentric radius, virial parameter with mass, velocity dispersion with mass and mass with radius. With ClumpFind we computed the following properties : velocity dispersion with mass, mass with radius and mass with galactocentric distance. With HOP we computed the following : virial parameter with mass, virial parameter with galactocentric distance and velocity dispersion with mass. The reason we computed different properties via different algorithms lies mostly on the fact that we wanted to investigate different properties than to compare the algorithms with themselves. Besides, in spite of which algorithm we used, the properties between the two models show no difference. This is not surprising because the magnetic field in model MHD is very weak. Future models with a stronger magnetic field are needed in order to investigate this question further.

The finding that the magnetised model forms more massive clouds is an indicator that the magnetic field boosts star formation. Indeed, we did find that

the magnetised model has a slightly higher SFR. The result that the magnetic field can enhance star formation is counter-intuitive, because many previous studies have shown the opposite to be true (Federrath, 2015; Seifried and Walch, 2015; Wurster et al., 2019; Hennebelle and Inutsuka, 2019; Wu et al., 2020). A study of why these differences arise is beyond the scope of this thesis.

Magnetic field can affect many properties molecular clouds (Hennebelle and Inutsuka, 2019). Nevertheless, from our analysis the conclusion that arises is that the magnetised and the un-magnetised model have the same properties. A suggestion would be that the magnetic field in model MHD is very weak. However, despite this fact and the fact that the properties of the molecular clouds are almost the same we did find differences in the gas distribution between the two models for all evolution times of the galaxy. Regarding the gas distribution, we observed that the magnetic field's intensity is higher at the GMCs densest regions. Moreover, it is interesting that in the central region a nuclear bar was forming and was evolving differently for both models as the time went by.

Regarding the cloud identification, we observe several differences between the algorithms that we used. To begin with, as we mentioned above, the effectiveness of Dendrogram relies on resolution. The algorithm finds more clouds as the resolution increases. Furthermore, as we observe from figures 3.11, 3.12, and 3.13, the lower the resolution, the more scattered from the center are the identified GMCs. We do not have any reason to believe that Clumpfind would have a different behavior because both algorithms need the data to be interpolated on a uniform grid. While HOP and Clumpfind identify clouds within a similar mass range ($4.5M_{\odot} < M_{cl} < 7M_{\odot}$), Dendrogram (at the same resolution as Clumpfind) misses the lowest-mass clouds, as we can see from a simple visual inspection of Figures 2.4 and 2.5. This probably comes from our choices for the peak height in Dendrogram, but we have not investigated a wide range of parameters here.

Also, HOP's clouds have higher velocity dispersions compared to those of Dendrogram, but both HOP and Clumpfind find approximately the same values within the scatter. Moreover,the distributions of all the algorithms tend to be compatible with the second Larson's relation (eq.1.3).

Another property investigated for both Dendrogram and HOP is the relation of the virial parameter as a function of mass. Comparing the two distributions from the two algorithms we come to conclusion that, HOP finds more massive clouds which are more stable than those found by Dendrogram.

Further, we have examined the mass as a function of galactocentric distance (Figures 3.15, 3.22). Comparing figures 3.15 and 3.22 we see that for both algorithms a high percentage of the molecular clouds are found around 1 kpc.

Finally, we looked at the mass of the cloud as a function of its radius. Figures 3.19 and 3.21 show that the mass-radius relation is consistent between Dendrogram and Clumpfind, apart from the difference in masses mentioned above.

In conclusion, we could not find a physical explanation for the higher SFR and excess of dense gas in model MHD. But we did find that a weak magnetic field such as the one in the MHD simulation, does not affect the properties of the molecular clouds. Moreover, even if we could not explain the reason, we found

that the magnetic field plays a role in the star formation process and actually it boosts it. If this results persists with higher-resolution models, including more physics, it will be particularly interesting.

# Chapter 5

# Conclusions

In this work, we have presented an analysis of the dense gas and molecular clouds in two numerical MHD simulations of Milky- Way - like galaxies. Of the two models, one is magnetised (model MHD) and the other is not (model HYDRO).

The first difference we note in our analysis is that the distribution of the dense gas evolves differently in time for the two models. In particular, model MHD has more dense gas. Investigating this, we found that model MHD forms slightly more massive clouds. Moreover, from a SFR analysis we found that model MHD has a slightly higher SFR than model HYDRO as the galaxy evolves in time.

In order to understand why the SFR of model MHD is higher, we identified and studied the molecular clouds for both models because molecular clouds are the star nurseries of a galaxy. For cloud identification we used three different algorithms. The last algorithm, HOP, was the more effective in identifying clouds.

Having identified the molecular clouds, we calculated some statistical properties such as: velocity dispersion as a function of mass, mass of the cloud as a function of its radius, mass of the cloud as a function of the galactocentrinc distance and velocity dispersion as a function of the galactocentrinc distance. The result was that every property was similar for both models.

To conclude, even though we found that the magnetised model forms more massive clouds and has a higher SFR, the cloud properties of both models show no deviation. Further modeling with more detailed sub-grid physics and a larger range of magnetic field strengths are needed in order to understand these differences better.

# Bibliography

P. André, A. Men'shchikov, S. Bontemps, V. Könyves, F. Motte, N. Schneider, P. Didelon, V. Minier, P. Saraceno, D. Ward-Thompson, J. di Francesco, G. White, S. Molinari, L. Testi, A. Abergel, M. Griffin, T. Henning, P. Royer, B. Merín, R. Vavrek, M. Attard, D. Arzoumanian, C. D. Wilson, P. Ade, H. Aussel, J. P. Baluteau, M. Benedettini, J. P. Bernard, J. A. D. L. Blommaert, L. Cambrésy, P. Cox, A. di Giorgio, P. Hargrave, M. Hennemann, M. Huang, J. Kirk, O. Krause, R. Launhardt, S. Leeks, J. Le Pennec, J. Z. Li, P. G. Martin, A. Maury, G. Olofsson, A. Omont, N. Peretto, S. Pezzuto, T. Prusti, H. Roussel, D. Russeil, M. Sauvage, B. Sibthorpe, A. Sicilia-Aguilar, L. Spinoglio, C. Waelkens, A. Woodcraft, and A. Zavagno. From filamentary clouds to prestellar cores to the stellar IMF: Initial highlights from the Herschel Gould Belt Survey. , 518:L102, July 2010. doi: 10.1051/0004-6361/201014666.

R. Beck. Magnetic fields and interstellar gas clouds in the spiral galaxy NGC 6946. , 251:15, Nov. 1991.

R. Beck, A. Brandenburg, D. Moss, A. Shukurov, and D. Sokoloff. Galactic Magnetism: Recent Developments and Perspectives. , 34:155–206, Jan. 1996. doi: 10.1146/annurev.astro.34.1.155.

F. Bertoldi and C. F. McKee. Pressure-confined Clumps in Magnetized Molecular Clouds. , 395:140, Aug. 1992. doi: 10.1086/171638.

K. Beuermann, G. Kanbach, and E. M. Berkhuijsen. Radio structure of the Galaxy: thick disk and thin disk at 408 MHz. , 153:17–34, Dec. 1985.

S. B. Charnley. Hot Core Chemistry. , 224(1-2):251–254, Feb. 1995. doi: 10.1007/BF00667853.

R. M. Crutcher. Magnetic Fields in Molecular Clouds: Observations Confront Theory. , 520(2):706–713, Aug. 1999. doi: 10.1086/307483.

D. J. Eisenstein and P. Hut. HOP: A New Group-Finding Algorithm for N-Body Simulations. , 498(1):137–142, May 1998. doi: 10.1086/305535.

E. Falgarone and T. G. Phillips. A Signature of the Intermittency of Interstellar Turbulence: The Wings of Molecular Line Profiles. , 359:344, Aug. 1990. doi: 10.1086/169068.

C. Federrath. Inefficient star formation through turbulence, magnetic fields and feedback. , 450(4):4035–4042, July 2015. doi: 10.1093/mnras/stv941.

A. Fletcher, R. Beck, A. Shukurov, E. M. Berkhuijsen, and C. Horellou. Magnetic fields and spiral arms in the galaxy M51. , 412(4):2396–2416, Apr. 2011. doi: 10.1111/j.1365-2966.2010.18065.x.

S. Fromang, P. Hennebelle, and R. Teyssier. A high order Godunov scheme with constrained transport and adaptive mesh refinement for astrophysical magnetohydrodynamics. , 457(2):371–384, Oct. 2006. doi: 10.1051/0004-6361:20065371.

G. M. Green, E. F. Schlafly, D. P. Finkbeiner, H.-W. Rix, N. Martin, W. Burgett, P. W. Draper, H. Flewelling, K. Hodapp, N. Kaiser, R. P. Kudritzki, E. Magnier, N. Metcalfe, P. Price, J. Tonry, and R. Wainscoat. A Three-dimensional Map of Milky Way Dust. , 810(1):25, Sept. 2015. doi: 10.1088/0004-637X/810/1/25.

J. L. Han and J. S. Zhang. The Galactic distribution of magnetic fields in molecular clouds and HII regions. , 464(2):609–614, Mar. 2007. doi: 10.1051/0004-6361:20065801.

P. Hennebelle and S.-i. Inutsuka. The role of magnetic field in molecular cloud formation and evolution. *Frontiers in Astronomy and Space Sciences*, 6:5, Mar. 2019. doi: 10.3389/fspas.2019.00005.

J. H. Jeans. The Stability of a Spherical Nebula. *Philosophical Transactions of the Royal Society of London Series A*, 199:1–53, Jan. 1902. doi: 10.1098/rsta.1902.0012.

I. Kazes, T. H. Troland, R. M. Crutcher, and C. Heiles. The Magnetic Field in the Vicinity of S106. , 335:263, Dec. 1988. doi: 10.1086/166924.

J. Kennicutt, Robert C. The Global Schmidt Law in Star-forming Galaxies. , 498(2):541–552, May 1998. doi: 10.1086/305588.

R. C. Kennicutt and N. J. Evans. Star Formation in the Milky Way and Nearby Galaxies. , 50:531–608, Sept. 2012. doi: 10.1146/annurev-astro-081811-125610.

A. G. Kritsuk, S. D. Ustyugov, M. L. Norman, and P. Padoan. Simulations of Supersonic Turbulence in Molecular Clouds: Evidence for a New Universality. In N. V. Pogorelov, E. Audit, P. Colella, and G. P. Zank, editors, *Numerical Modeling of Space Plasma Flows: ASTRONUM-2008*, volume 406 of *Astronomical Society of the Pacific Conference Series*, page 15, Apr. 2009.

T. Kudoh and S. Basu. Three-dimensional Simulation of Magnetized Cloud Fragmentation Induced by Nonlinear Flows and Ambipolar Diffusion. , 679 (2):L97, June 2008. doi: 10.1086/589618.

R. B. Larson. Turbulence and star formation in molecular clouds. , 194:809–826, Mar. 1981. doi: 10.1093/mnras/194.4.809.

E. L. Łokas and G. A. Mamon. Properties of spherical galaxies and clusters with an NFW density profile. , 321(1):155–166, Feb. 2001. doi: 10.1046/j.1365-8711.2001.04007.x.

F. Louvet, P. Hennebelle, A. Men'shchikov, P. Didelon, E. Ntormousi, and F. Motte. Strong dependence of the physical properties of cores on spatial resolution in observations and simulations. , 653:A157, Sept. 2021. doi: 10.1051/0004-6361/202040053.

F. Massi, A. Weiss, D. Elia, T. Csengeri, E. Schisano, T. Giannini, T. Hill, D. Lorenzetti, K. Menten, L. Olmi, F. Schuller, F. Strafella, M. De Luca, F. Motte, and F. Wyrowski. Dense cores and star formation in the giant molecular cloud Vela C. , 628:A110, Aug. 2019. doi: 10.1051/0004-6361/201935047.

C. F. McKee and J. P. Ostriker. A theory of the interstellar medium: three components regulated by supernova explosions in an inhomogeneous substrate. , 218:148–169, Nov. 1977. doi: 10.1086/155667.

A. Men'shchikov, P. André, P. Didelon, V. Könyves, N. Schneider, F. Motte, S. Bontemps, D. Arzoumanian, M. Attard, A. Abergel, J. P. Baluteau, J. P. Bernard, L. Cambrésy, P. Cox, J. di Francesco, A. M. di Giorgio, M. Griffin, P. Hargrave, M. Huang, J. Kirk, J. Z. Li, P. Martin, V. Minier, M. A. Miville-Deschênes, S. Molinari, G. Olofsson, S. Pezzuto, H. Roussel, D. Russeil, P. Saraceno, M. Sauvage, B. Sibthorpe, L. Spinoglio, L. Testi, D. Ward-Thompson, G. White, C. D. Wilson, A. Woodcraft, and A. Zavagno. Filamentary structures and compact objects in the Aquila and Polaris clouds observed by Herschel. , 518:L103, July 2010. doi: 10.1051/0004-6361/201014668.

M. A. Miville-Deschênes, N. Ysard, A. Lavabre, N. Ponthieu, J. F. Macías-Pérez, J. Aumont, and J. P. Bernard. Separation of anomalous and synchrotron emissions using WMAP polarization data. , 490(3):1093–1102, Nov. 2008. doi: 10.1051/0004-6361:200809484.

T. C. Mouschovias and J. Spitzer, L. Note on the collapse of magnetic interstellar clouds. , 210:326, Dec. 1976. doi: 10.1086/154835.

J. F. Navarro, C. S. Frenk, and S. D. M. White. The Structure of Cold Dark Matter Halos. , 462:563, May 1996. doi: 10.1086/177173.

S. Niklas. PhD thesis, -, Jan. 1995.

E. Ntormousi. Magnetic fields in massive spirals: The role of feedback and initial conditions. , 619:L5, Nov. 2018. doi: 10.1051/0004-6361/201834153.

E. Ntormousi, K. Tassis, F. Del Sordo, F. Fragkoudi, and R. Pakmor. A dynamo amplifying the magnetic field of a Milky-Way-like galaxy. , 641:A165, Sept. 2020. doi: 10.1051/0004-6361/202037835.

V. Perret. DICE: Disk Initial Conditions Environment, July 2016.

V. Perret, F. Renaud, B. Epinat, P. Amram, F. Bournaud, T. Contini, R. Teyssier, and J. C. Lambert. Evolution of the mass, size, and star formation rate in high redshift merging galaxies. MIRAGE - A new sample of simulations with detailed stellar feedback. , 562:A1, Feb. 2014. doi: 10.1051/0004-6361/201322395.

M. J. Rees. The origin and cosmogonic implications of seed magnetic fields. , 28:197–206, Sept. 1987.

M. Schmidt. The Rate of Star Formation. , 129:243, Mar. 1959. doi: 10.1086/146614.

P. Scicluna and R. Siebenmorgen. Extinction and dust properties in a clumpy medium. , 584:A108, Dec. 2015. doi: 10.1051/0004-6361/201323149.

D. Seifried and S. Walch. The impact of turbulence and magnetic field orientation on star-forming filaments. , 452(3):2410–2422, Sept. 2015. doi: 10.1093/mnras/stv1458.

M. Simard-Normandin and P. P. Kronberg. Rotation measures and the galactic magnetic field. , 242:74–94, Nov. 1980. doi: 10.1086/158445.

J. D. Soler, P. Hennebelle, P. G. Martin, M. A. Miville-Deschênes, C. B. Netterfield, and L. M. Fissel. An Imprint of Molecular Cloud Magnetization in the Morphology of the Dust Polarized Emission. , 774(2):128, Sept. 2013. doi: 10.1088/0004-637X/774/2/128.

R. S. Sutherland and M. A. Dopita. Cooling Functions for Low-Density Astrophysical Plasmas. , 88:253, Sept. 1993. doi: 10.1086/191823.

R. Teyssier. Cosmological hydrodynamics with adaptive mesh refinement. A new high resolution code called RAMSES. , 385:337–364, Apr. 2002. doi: 10.1051/0004-6361:20011817.

J. P. Williams, L. Blitz, and C. F. McKee. The Structure and Evolution of Molecular Clouds: from Clumps to Cores to the IMF. In V. Mannings, A. P. Boss, and S. S. Russell, editors, *Protostars and Planets IV*, page 97, May 2000.

B. Wu, J. C. Tan, D. Christie, and F. Nakamura. GMC Collisions as Triggers of Star Formation. VII. The Effect of Magnetic Field Strength on Star Formation. , 891(2):168, Mar. 2020. doi: 10.3847/1538-4357/ab77b5.

J. Wurster, M. R. Bate, and D. J. Price. There is no magnetic braking catastrophe: low-mass star cluster and protostellar disc formation with non-ideal magnetohydrodynamics. , 489(2):1719–1741, Oct. 2019. doi: 10.1093/mnras/stz2215.

B. Zuckerman and P. Palmer. Radio radiation from interstellar molecules. , 12: 279–313, Jan. 1974. doi: 10.1146/annurev.aa.12.090174.001431.

# Chapter 6

# Appendices

A closer look to the molecular clouds in sub galactic scales will offer a better overview of the cloud morphology and distribution as the galaxy evolves in time. For this reason we plotted two more regions of the galaxy and zoomed in the sub galactic medium.

### 6.0.1 Upper right region

In this subsection we present the gas distribution in the upper right region of the galactic plane hereafter *Region 1* . Similar to figures in the previous subsection, they show the total column density of hydrogen in x-y galactic plane.

Figure 6.1 shows the galactic region studied here, in 587 Myr. Comparing the two models it does not seem to have many differences. Probably, it's worthy to mention that observing the 4 kpc run, MHD model has more dense cores than HYDRO and also the first one has a supernova.

The two models are quite similar in 867 and 1019 Myr as Figures 6.2 and 6.3 show.

In Figure 6.4 the most dense cores of HYDRO have been assembled in a region of 6.7 kpc left in x axis of galactic plane, in contrast with MHD where cores are scattered.

Model MHD in 2027 Myr has more dense cores than HYDRO (Figure 6.5).

### 6.0.2 Upper left region

Similar to the previous subsection, the region studied is the upper left of the galactic plane, hereafter *Region 2*.

Even though, at 587, 1019, 1529 and 2027 Myr *Region 2* (Figure 6.6, 6.8, 6.9 and 6.10) respectively) has more massive cores in model MHD, the gas distribution appears to be the same. On the contrary, at 867 Myr the two models seem quite similar (Figure 6.7).

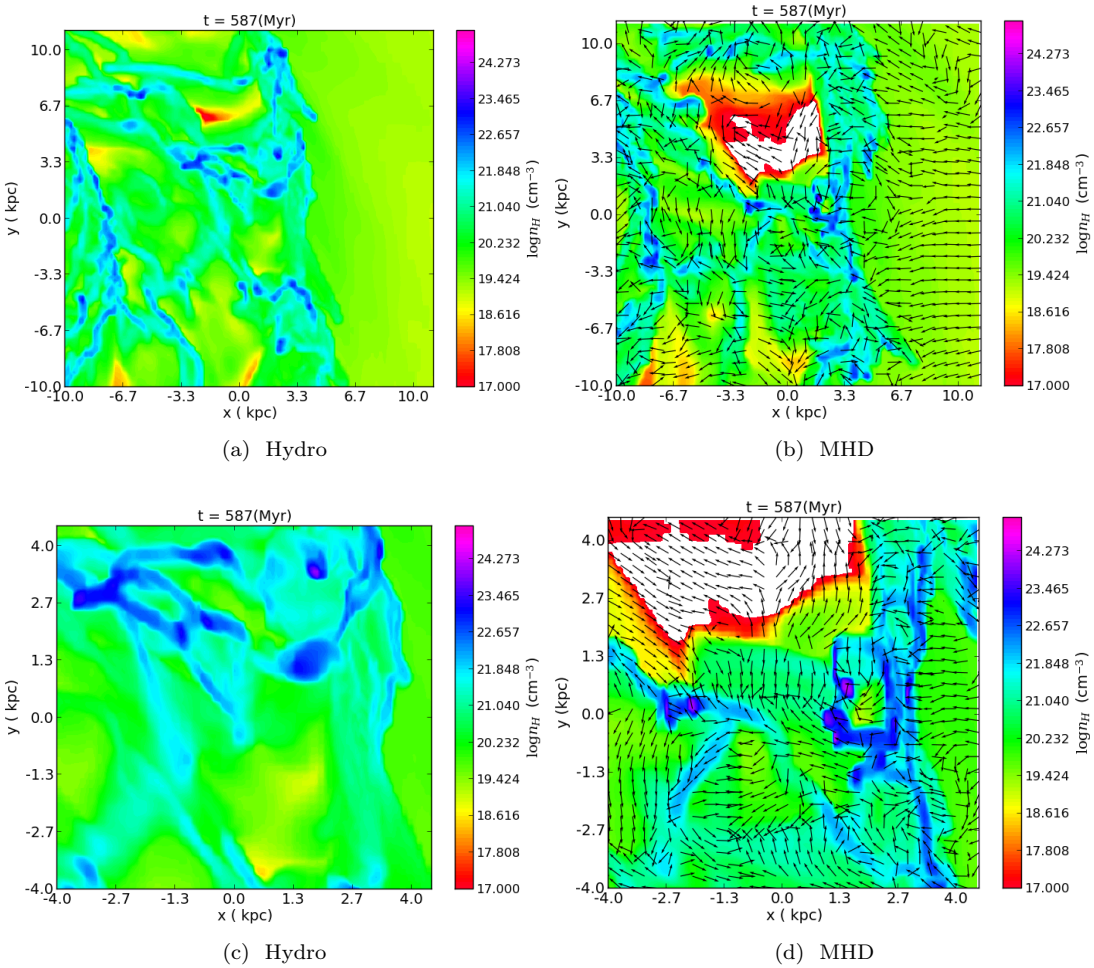


(a) Hydro (b) MHD

(c) Hydro (d) MHD

Figure 6.1: Similar to Fig.2, but the simulated region is the upper right side of the galaxy.

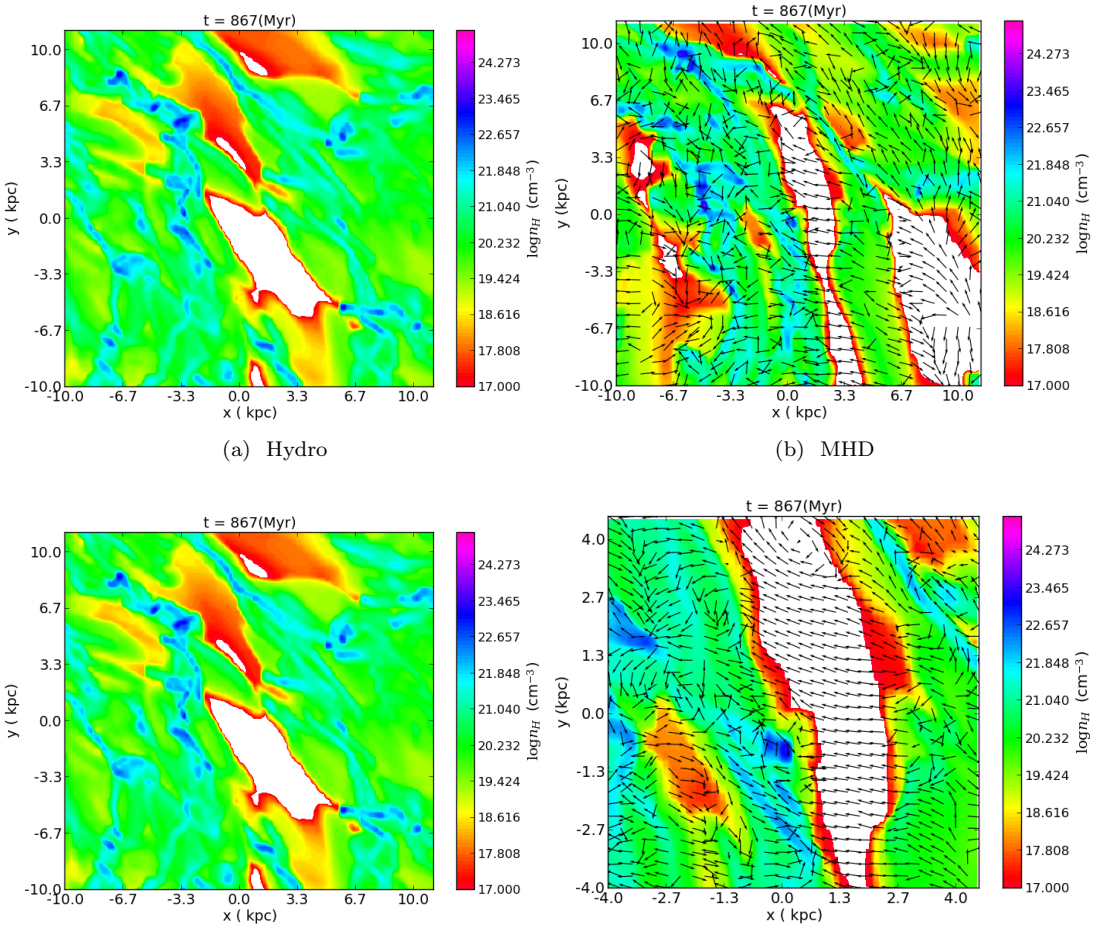


(a) Hydro

(b) MHD

(c) Hydro

(d) MHD

Figure 6.2: Similar to Fig.9

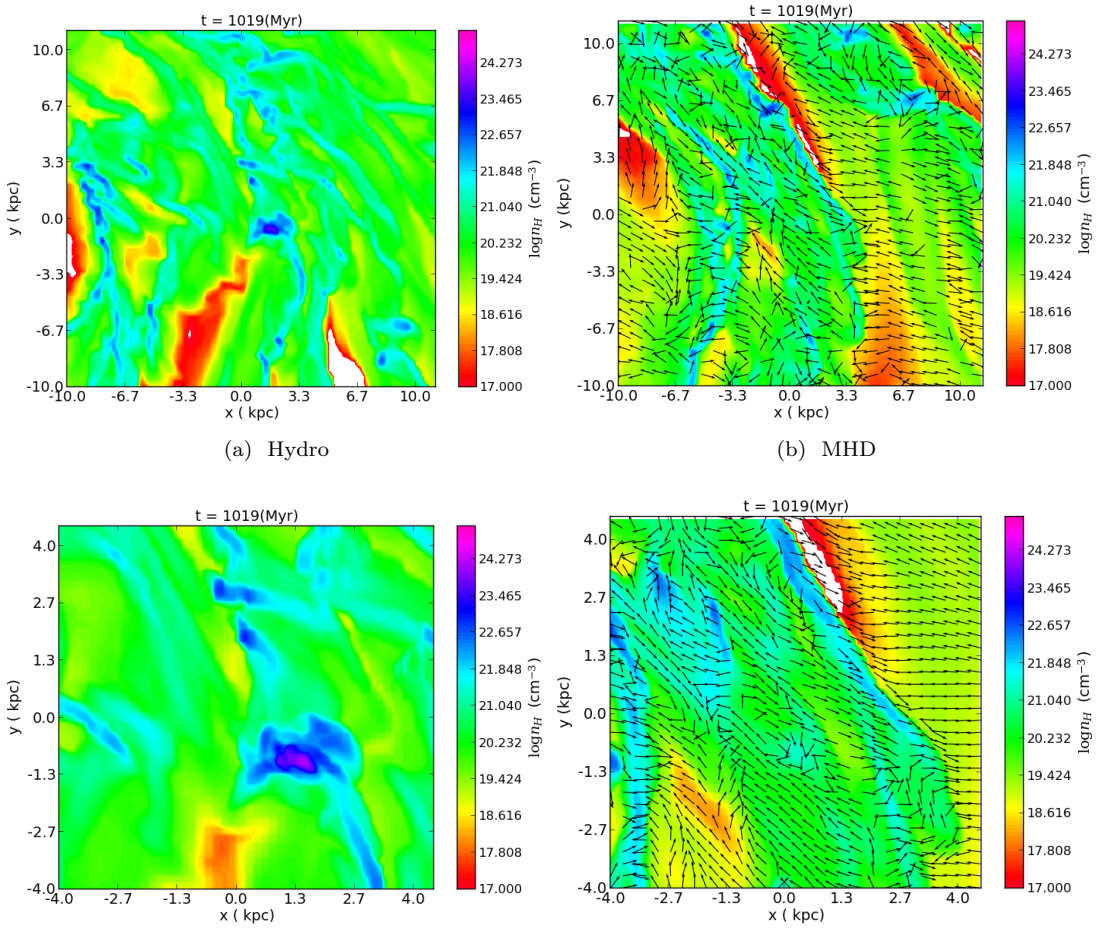


(a) Hydro (b) MHD

(c) Hydro (d) MHD

Figure 6.3: Similar to Fig.9,

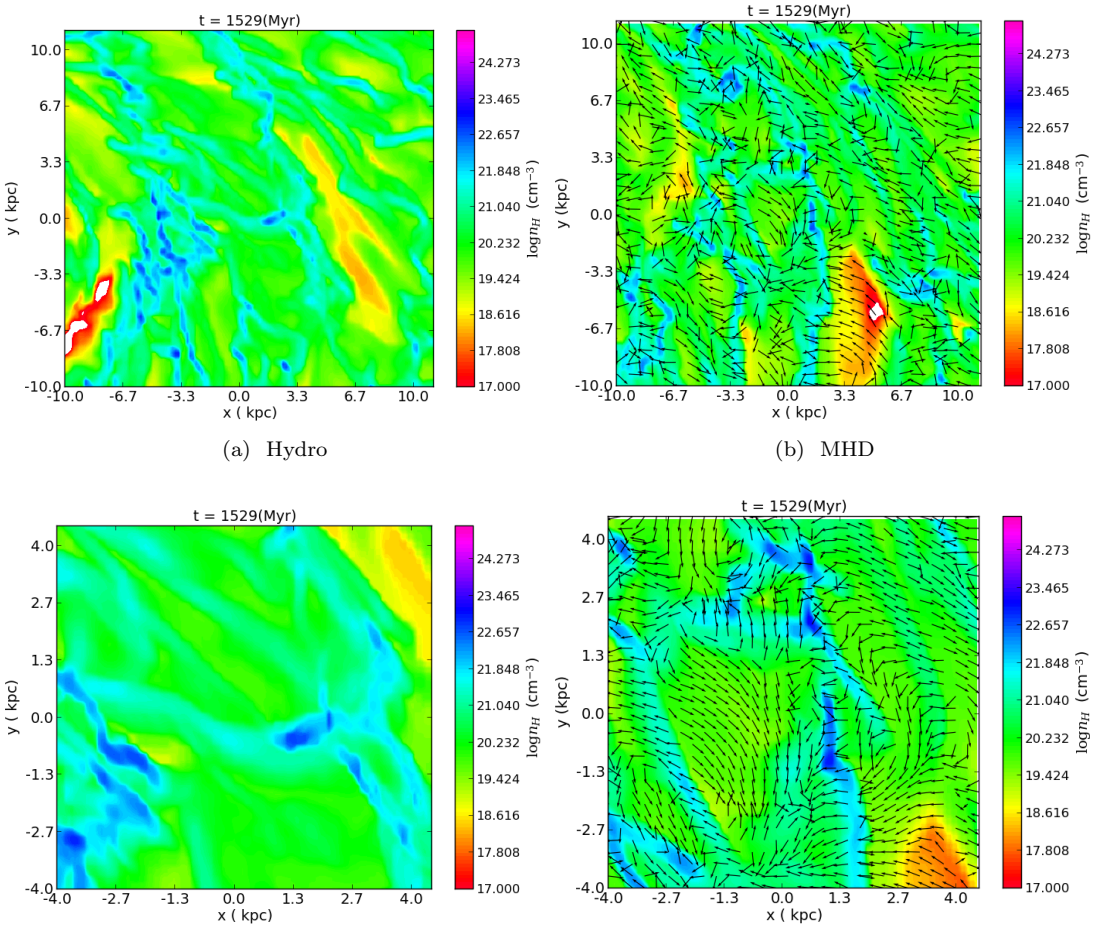


(a) Hydro (b) MHD

(c) Hydro (d) MHD

Figure 6.4: Similar to Fig.9,

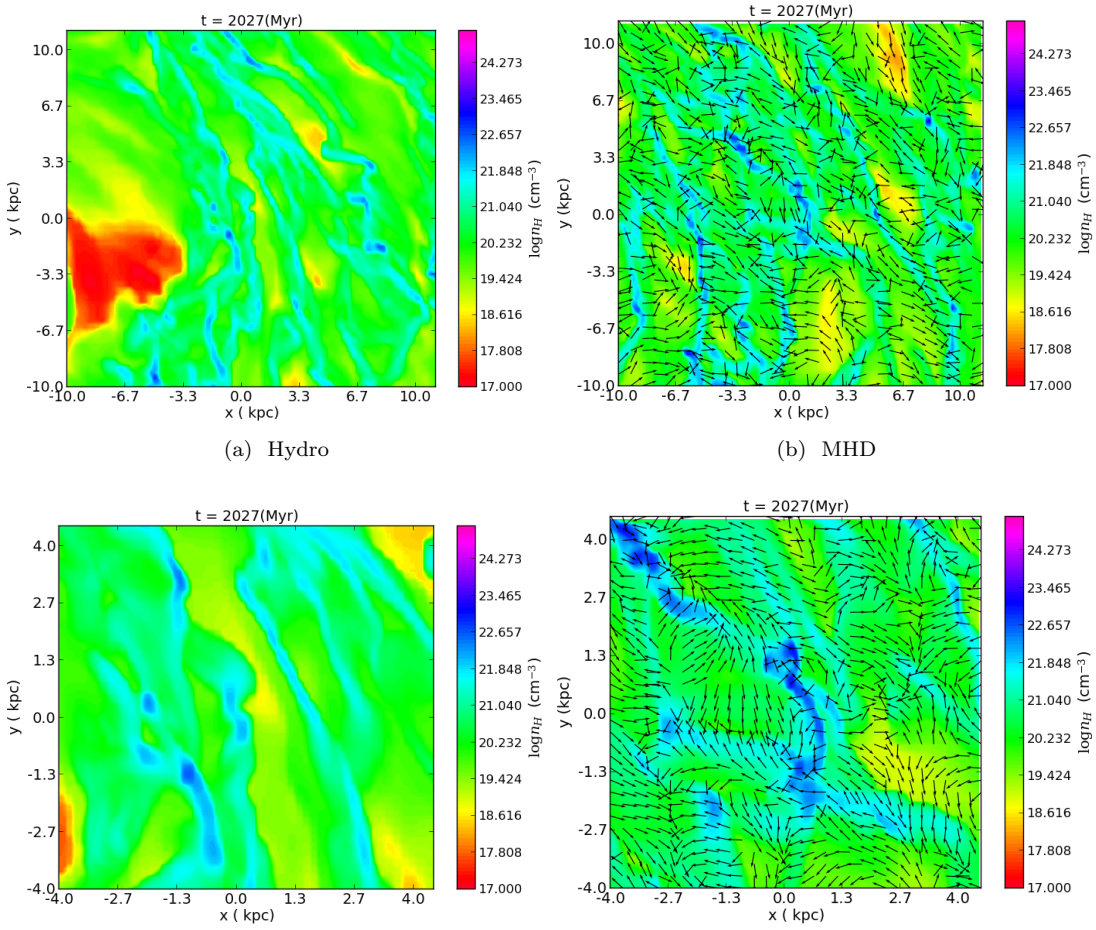


(a) Hydro (b) MHD

(c) Hydro (d) MHD

Figure 6.5: Similar to Fig.9,

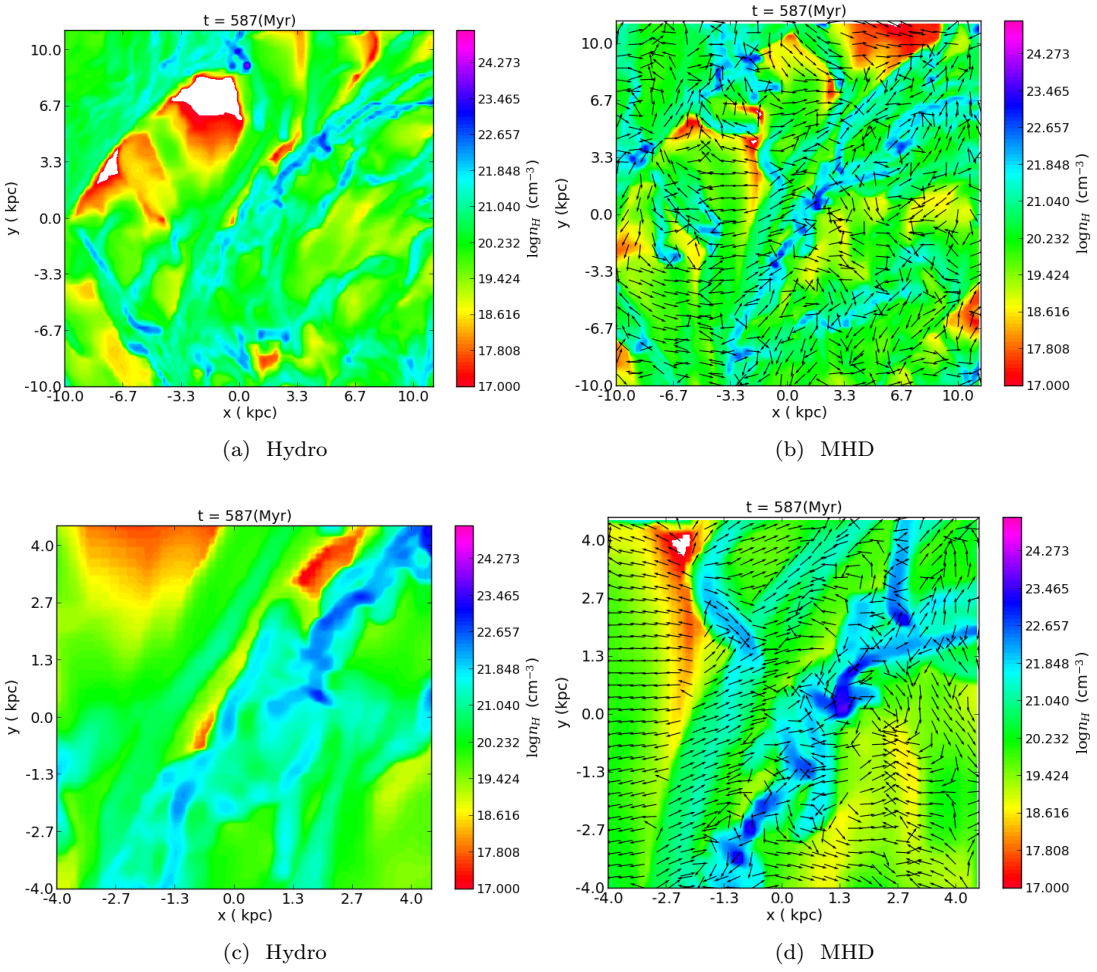


(a) Hydro (b) MHD

(c) Hydro (d) MHD

Figure 6.6: Similar to Fig.9,but the simulated region is the upper left side of the galaxy.

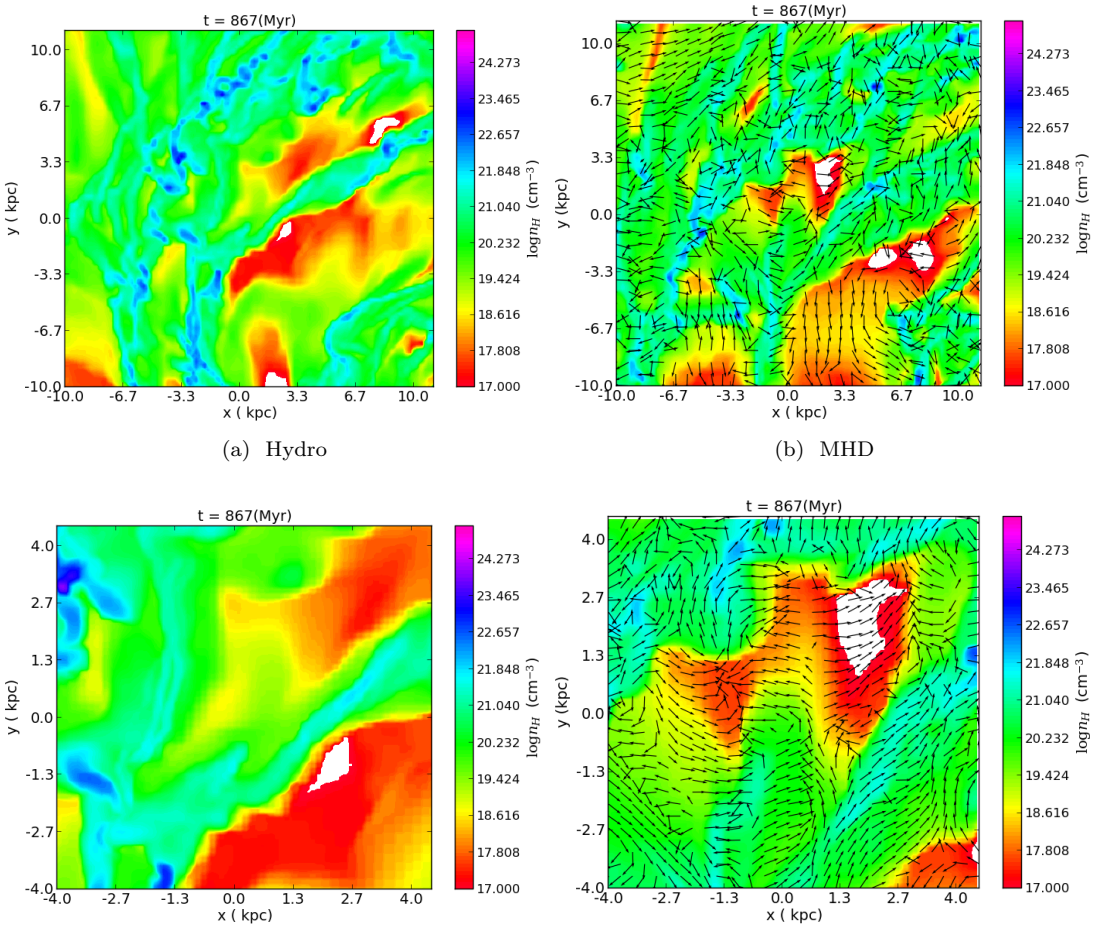


(a) Hydro (b) MHD

(c) Hydro (d) MHD

Figure 6.7: Similar to Fig.9,

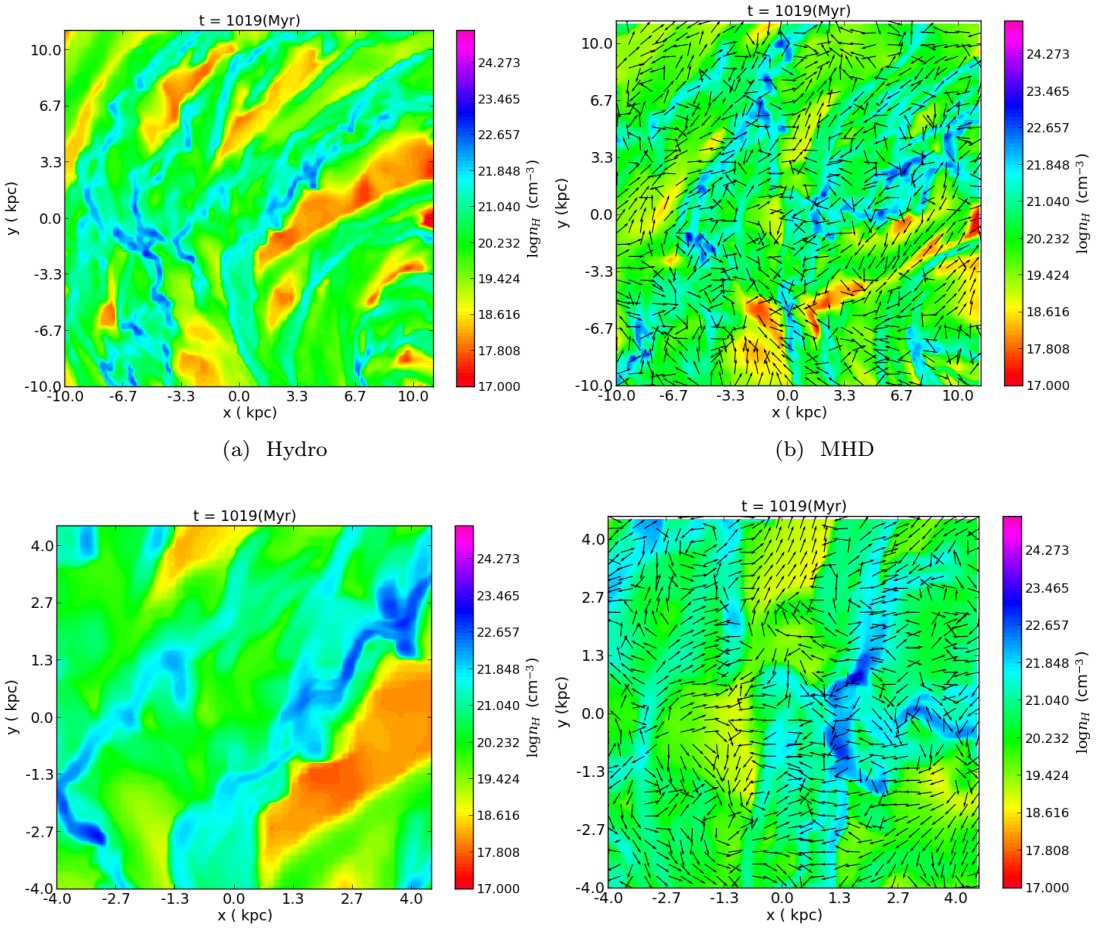


(a) Hydro

(b) MHD

(c) Hydro

(d) MHD

Figure 6.8: Similar to Fig.9,

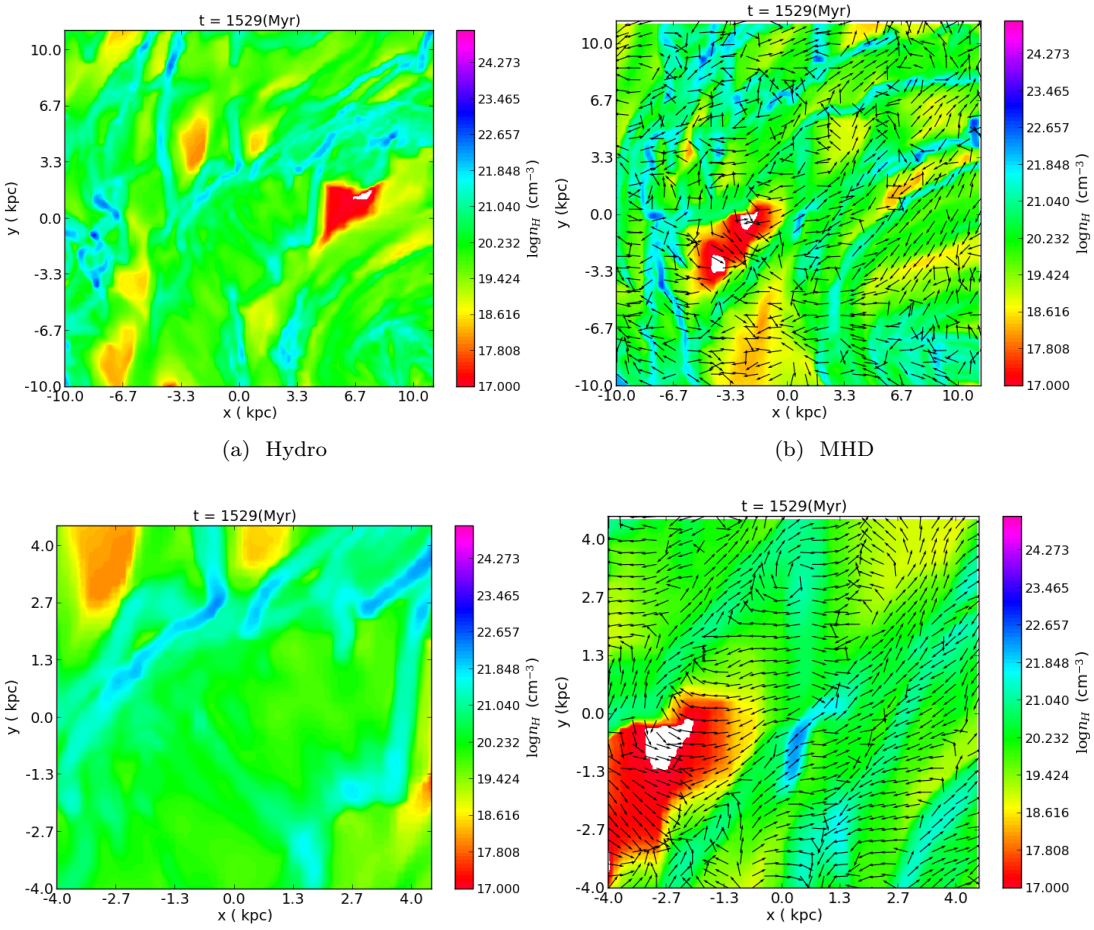


(a) Hydro (b) MHD

(c) Hydro (d) MHD

Figure 6.9: Similar to Fig.9,

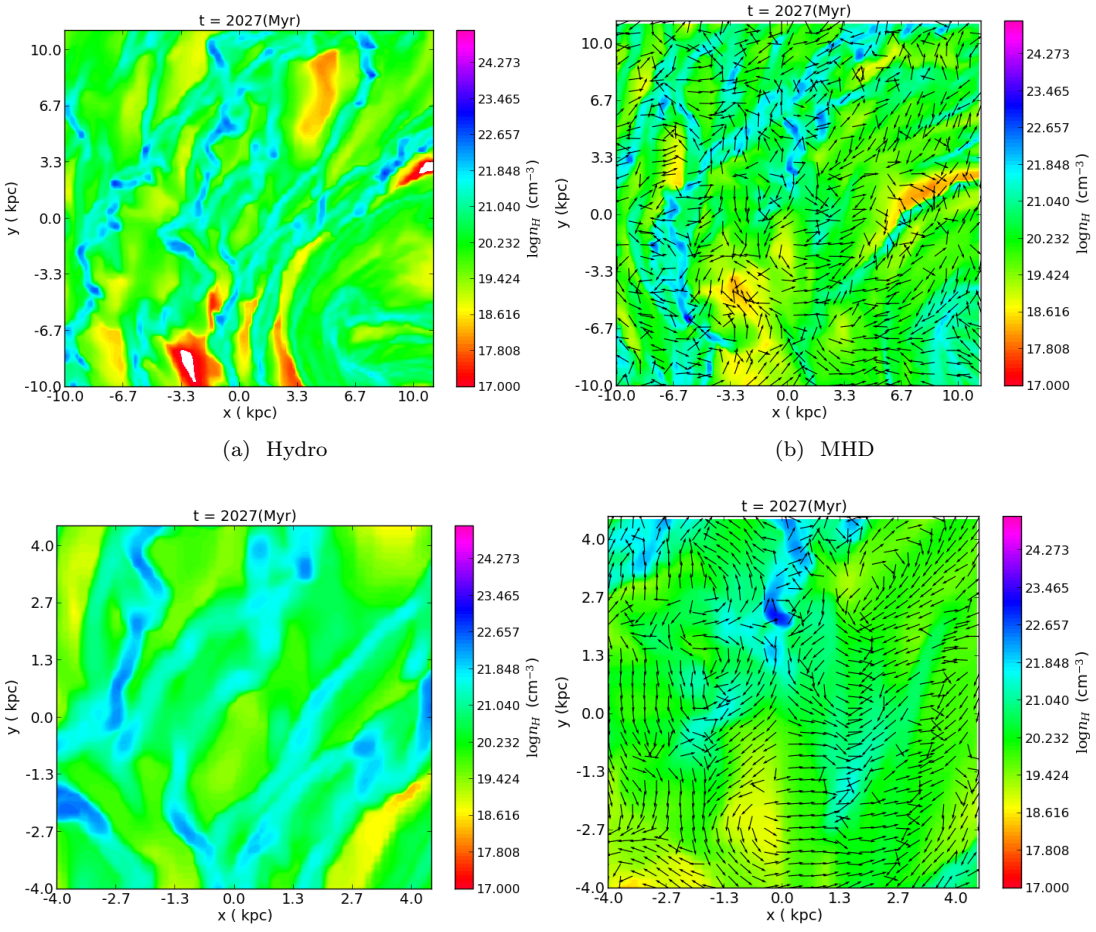


(a) Hydro (b) MHD

(c) Hydro (d) MHD

Figure 6.10: Similar to Fig.9,